2014

IN-SITU TEM PLASMA CHIP NANOFABRICATION AND CHARACTERIZATION

Xuebo Cui
Michigan Technological University

IN-SITU TEM PLASMA CHIP NANOFABRICATION AND CHARACTERIZATION

By
Xuebo Cui

A Thesis
Submitted in partial fulfillment of the requirements for the degree of
MASTER OF SCIENCE
In Mechanical Engineering

MICHIGAN TECHNOLOGICAL UNIVERSITY
2014

This thesis has been approved in partial fulfillment of the requirements for the Degree of MASTER OF SCIENCE in Mechanical Engineering.

Department of Mechanical Engineering-Engineering Mechanics

Report Advisor:	*Reza Shahbazian-Yassar*
Committee Member:	*Craig Friedrich*
Committee Member:	*Farzad Mashayek*
Department Chair:	*William W. Predebon*

To my parents Mr. Shiyuan Cui and Ms. Chunlian Guo

Table of Contents

Acknowledgements

The author acknowledges support from Dr. Reza Shahabazian-Yassar, ENS lab members Fei Long, Yu Zhao, Wentao Yao, and alumni lab member Qi Gao. Author also acknowledges the direction on plasma physics from Dr. L. Brad King.

The author also acknowledges help with cleanroom equipment training from Ph.D. students Radheshyam Tewari, Sterling prince, Jen-Yung Chang, and staff member William Kunderson at Michigan Technological University.

The majority of the nano-fabrication work was completed in the Nano Fabrication Center (NFC) at the University of Minnesota-Twin Cities. The author expresses sincere appreciation for NFC staff members: Paul Kimani, Kevin Roberts, and Tony Whipple, for their guidance and advice.

List of Abbreviations

CVD	Chemical Vapor Deposition
DC	Direct Current
DI water	De-ionized water
FEBID	Focused Electron Beam Induced Deposition
HMDS	Hexamethyldislazane
ICP	Inductively Coupled Plasma
LPCVD	Low Pressure Chemical Vapor Deposition
MWCNT	Multi Wall Carbon Nanotube
NFC	Nanofabrication Center in University of Minnesota at Twin City
PECVD	Plasma Enhanced Chemical Vapor Deposition
SEM	Scanning Electron Microscope
TEM	Transmission Electron Microscope
UV	Ultra-Violet Light

Abstract

A silicon-based microcell was fabricated with the potential for use in in-situ transmission electron microscopy (TEM) of materials under plasma processing. The microcell consisted of 50 nm-thick film of silicon nitride observation window with 60μm distance between two electrodes. E-beam scattering Mont Carlo simulation showed that the silicon nitride thin film would have very low scattering effect on TEM primary electron beam accelerated at 200 keV. Only 4.7% of primary electrons were scattered by silicon nitride thin film and the Ar gas (60 μm thick at 1 atm pressure) filling the space between silicon nitride films. Theoretical calculation also showed low absorption of high-energy e-beam electrons. Because the plasma cell needs to survive the high vacuum TEM chamber while holding 1 atm internal pressure, a finite element analysis was performed to find the maximum stress the low-stress silicon nitride thin film experienced under pressure. Considering the maximum burst stress of low-stress silicon nitride thin film, the simulation results showed that the 50 nm silicon nitride thin film can be used in TEM under 1 atm pressure as the observation window. Ex-situ plasma generation experiment demonstrated that air plasma can be ignited at DC voltage of 570. A Scanning electron microscopy (SEM) analysis showed that etching and deposition occurred during the plasma process and larger dendrites formed on the positive electrode.

1. Introduction

Plasma is the fourth state of matter after solid, liquid, and gas. As the temperature and energy level increase, matter transforms from solid to liquid to gas and finally reaches plasma status, which means electrons are no longer confined in their orbits and become free electrons. Electrons in chemical species can be excited and become free electrons by electron impact, photoionization, and heavy particle collision (***Fig.1.1***).[1] After excitation, the original chemical species become positive ion and negative electron pairs.

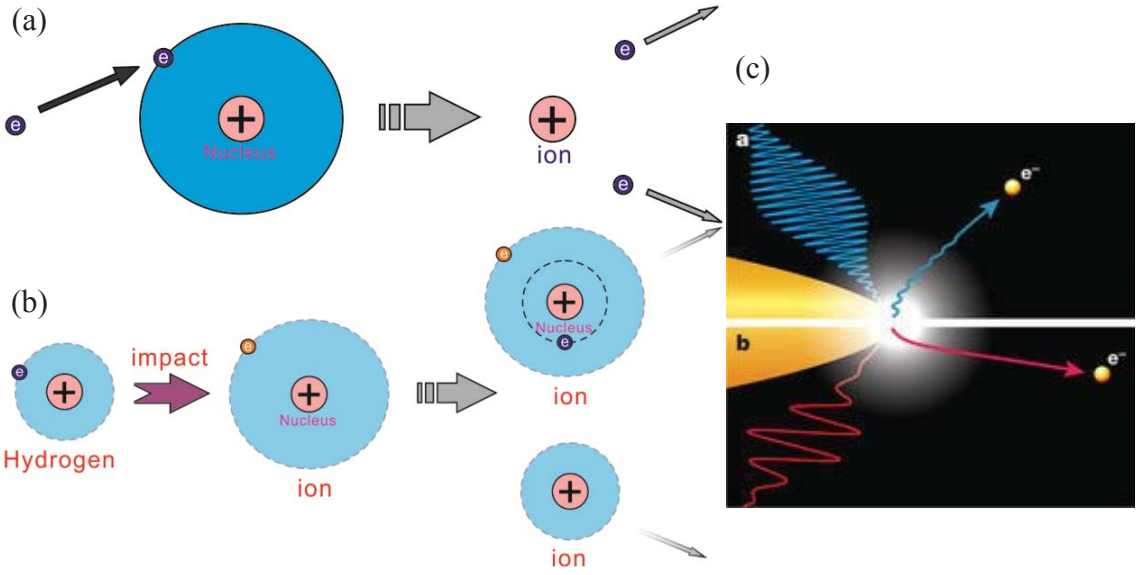

Fig. 1.1 *Major types of ionization processes (a) ionization by incident electron impact (b) ionization by heavy particle collision (c) ionization by photoionization and surface emission;*[2] *Reprinted by permission from Macmillan Publishers Ltd: Nature, G. Herink, D. R. Solli, M. Gulde, and C. Ropers, "Field-driven photoemission from nanostructures quenches the quiver motion," Nature, vol. 483, pp. 190-193, 03/08/print 2012., copyright 2012 NPG*

Plasma can be divided into two subclasses, cold plasma and hot plasma. Although there is no clear boundary between these two subclasses, people use these two names to refer to low energy plasma (electron temprature≤10eV) and high energy plasma (typically, electron temperature≥1eV).[3] Some people use cold plasma to refer to partially ionized matters and

use hot plasma to refer to matters that are completely ionized such as the plasma generated by fusion reaction (***Fig.1.2***).

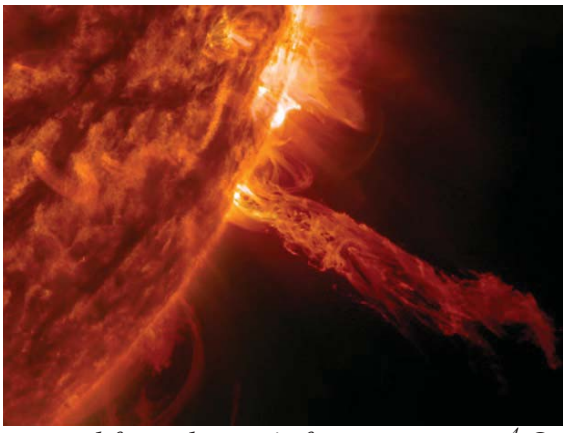

Fig.1.2 *plasma sputtered from the sun's fusion reaction.* [4] *© 2014 NASA*

Because of the ionized status of matter and plasma, plasma is widely used in industry for material processing, such as plasma etching, plasma enhanced chemical vapor deposition, (PECVD) and sputtering deposition. In scientific research, the importance of the role of plasma on synthesis nanostructures including nanotubes, nanowires, and nanoparticles is difficult to overstate.

1.1. Applications of plasma in material processing

Chemical species can be ionized and become reactive in a plasma environment. The benefit from easily controlled electrical field and electric force is that ions can be accelerated by the electric field and shoot against the etching target vertically.[5] Thus, trenches with a vertical sidewall can be fabricated using plasma etching. Recently, the directional property of inductively coupled plasma (ICP) etching was employed to fabricate trenches with a large depth-to-width ratio and smooth sidewall for device isolation purpose.[6-9] Furthermore, the etching selectivity and etching rate can be adjusted by a variety of ways, including alternate the chemical species composition, adjusting power supply to the plasma.[5,6]

The other significant advantage of the plasma process is that it can help reactions occur in relatively low temperature. The gas temperature can be controlled to lower than 150° in both plasma assisted etching and deposition.[10] This is a highly desired property in the semiconductor fabrication industry since many materials used are thermal sensitive including the process of wafers with photo-resistant material and patterns on them.[11] One good example is thin film structures, which can also be prepared by PECVD without overheating the substrate as seen in traditional Chemical Vapor Deposition (CVD) process.[11-13]

Plasma processes are also widely used in innovative material preparation including preparation of nanostructures such as silicon nanowire and multi-wall carbon nanotube (MWCNT).[14-16] In the preparation of CNT, the ion bombardment produced by the plasma can assist the surface reactions which lead to film growth and species product desorption.[16] In the work done by Sunkara et al., microwave-generated hydrogen plasma ignition was used to etch silicon substrate to provide vapor phase silyl radicals for growth of silicon nanowires.[15]

Plasma technologies are also used in air pollution control applications such as particle removal, odor elimination, CO_2 emission reduction, and volatile organic compounds (VOCs) decomposition applications.[17] Mizuno et al. presented a work to use partially discharged air to perform sterilization and deodorization. In Mizuno's work, an electrostatically augmented filter was built with a packed ferroelectric pellet layer. AC voltage was used to sustain a stable discharge while a DC corona discharge was used to precharge the dust particles. Thus the dust particles were collected by the pellet surface due to electric static force and subsequent plasma chemical reactions can kill bacteria and perform deodorization.[18]

1.2. The motivation for atomic scale observation of plasma processing

Although plasma processes have been widely employed by industry, some details of these processes remain unknown, such as the localized behaviors of atomic deposition behaviors under various plasma processing parameters. Much recent research requires knowledge on the atoms' landing behaviors and arranging order. One example is the landing site preference of nanoparticles in dusty plasma.[19,20] Localized atomic arrangement observation is also required to improve nanostructure and material synthesis. For example, the synthesis of Si nanowire usually incorporates undesired Au atoms and degrades the electric property of the semiconductor nanowire.[21] Obtaining the atomic resolution images of Au atom sites during plasma process can help researchers to understand the nanowire growing mechanics.[21] Experimentally conformed atomic configuration information of material is also desired to understand the atom arrangement in disordered materials in materials science and solid state physics fields.[22]

1.3. In-situ plasma processing in electron microscopy

Wilson et al. presented a micro-plasma generator which generates in-situ microplasma to etch the silicon wafer substrate (***Fig. 1.3***). The DC microplasma was generated in 1-20 torr SF_6 gas and the results also demonstrated the silicon etching rate is linearly related to the power density of the plasma.[23] Wilson's work demonstrated the possibility and usage of micro-sized plasma, but because of the limited system setup, the silicon substrate can only be characterized after experiments by using SEM (***Fig. 1.3 (b)***) and thus, etchant and substrate reaction details in real-time is lost.

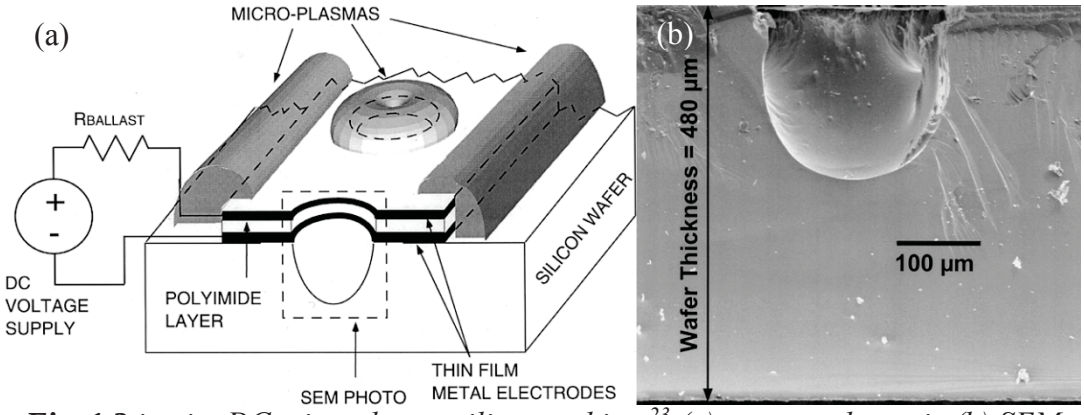

Fig. 1.3 *in-situ DC microplasma silicon etching [23] (a) system schematic (b) SEM characterization for localized silicon etching; credit to Wilson et al. © 2011 IEEE*

The effort made by Miyazoe et al. achieved real time observation of metal nanostructure in a high vacuum SEM chamber by Focused Electron Beam Induced Deposition (FEBID) assisted by a microplasma torch (***Fig. 1.4***). In this process, plasma acts as the medium to deliver energy to chemical species and improve metal content in fabricated dendrite than conventional FEBID. [24] This work also endorses the possibility for real-time observation of plasma material processing by electron microscope technology without disturbing the imaging electron beam.[24] Nevertheless, the resolution of the image is limited by SEM and it is also impossible for researchers to observe the atomic structure evolution of nanocone during the growing process.

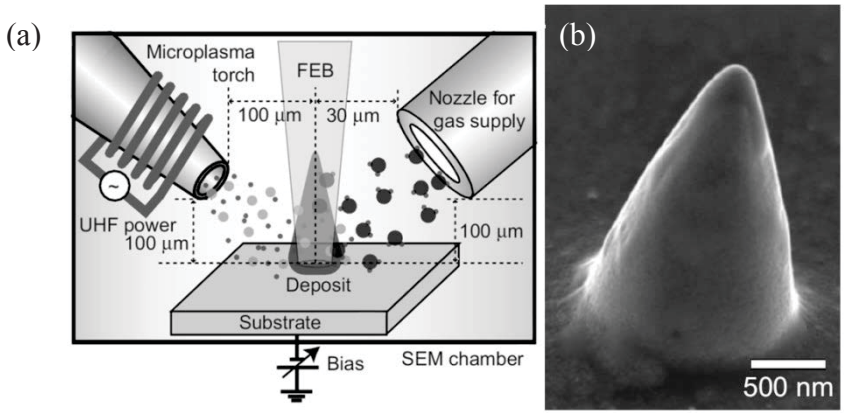

Fig. 1.4 *SEM conjuncts with microplasma torch for FEBID grow a metal nanostructure inside high vacuum SEM chamber [24] (a) the system setup and (b) grown nano cone structure with high metal contain; credit to Miyazoe et al.*

1.4. In-situ TEM for plasma experiments

Transmission electron microscope (TEM) is a kind of powerful tool that can provide detailed information about material structure in atomic scale and, furthermore, in-situ TEM methods can provide real time observation of nanostructure formation. These characters make TEM an outstanding candidate for localized plasma material process research.

To move any plasma process into a TEM chamber requires additional accessories. The TEM chamber is under high vacuum while operating to allow a high-energy electron beam to go straight through the target without interacting with gas molecules, which may scatter the electron beam and lower the imaging quality. So plasma cannot be generated directly in the TEM chamber (***Fig 1.5***).

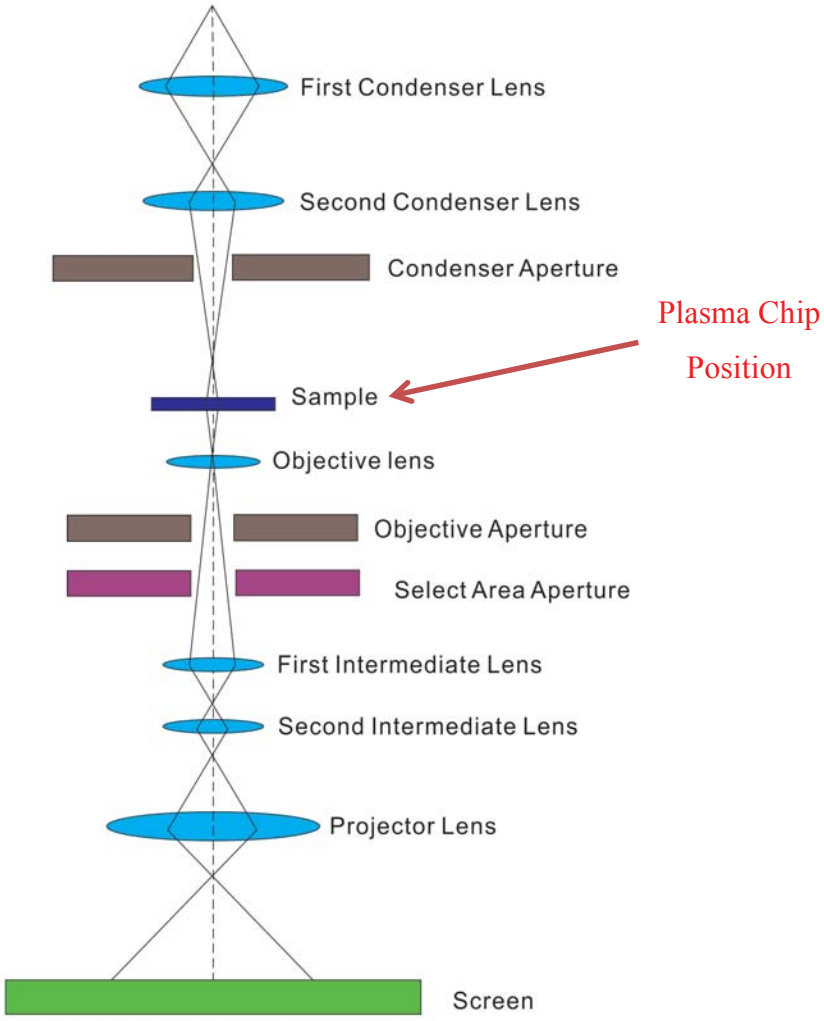

Fig.1.5 *Schematic of the TEM structure and its high energy electron beam path*

In 2011, Sun et al, reported a real time observation for ionized gas and sliver nanoparticle interaction in an environmental cell by using in-situ TEM method.[25] In this method, TEM was used to produce ionized gas and perform the observation at the same time. However, plasma is not generated and no extra circuit is used to excite the ionization process (***Fig. 1.6***). They used a silver-coated silicon nitride grid and an uncoated silicon nitride grid face to face and employed the unsmooth silver nanoparticles to form some nanocavities with thickness of 40-100nm in between. These cavities were used to enclose air in 1atm pressure by soaking the prepared grids in air for two days before the cavity sealing.[25] The 200keV-electron beam was used to induce ionic air gas in this cavity and the Ag grain morphology

was proven to evolution with a relation to the TEM beam current.[25] By using Monte Carlo simulation, the authors showed primary electrons from the TEM electron beam were not the direct source of ionization of the air gas, because it has a very high energy and scattered electrons with lower energy can be easily captured by AgO nanoparticles.[25] The in-situ TEM observation also provided the local crystallographic texture evolution information of Ag nanoparticles by collecting their diffraction pattern. The intensity of the diffraction rings provide the volume ratio change of Ag and AgO in some nanoparticles and information about oxidation and reduction induced by the e beam.[25] It was shown that when beam current density is under $0.2A \cdot cm^{-2}$ silver grains tend to have migration behavior that move apart from each other and diffraction pattern showed the existent of Ag_2O and AgO. When the beam current exceed $0.65A \cdot cm^{-2}$, Ag_2O phase structures will be oxidized to AgO.[25]

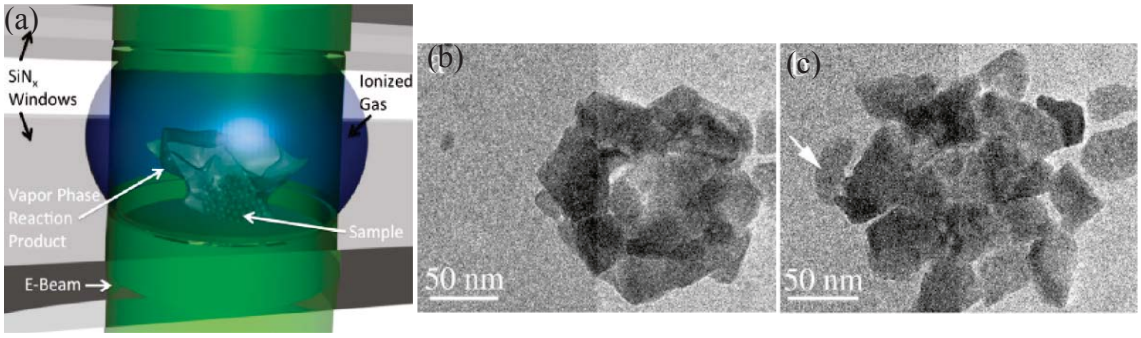

Fig. 1.6 *In-situ TEM observation for Ag oxidation (a) TEM electron beam was used to ionize gas and observing sliver particle oxidation in an environmental cell. Compare (b) and (c), under the effect of TEM electron beam, a sliver grain was found formed as pointed by the white arrow in (c).* [25] *Reprinted with permission from L. Sun, K. W. Noh, J.-G. Wen, and S. J. Dillon, "In Situ Transmission Electron Microscopy Observation of Silver Oxidation in Ionized/Atomic Gas," Langmuir, vol. 27, pp. 14201-14206, 2011/12/06 2011.Copyright2011, American Chemical Society*

Very recently, a novel method for real-time in-situ TEM observation of plasma material processing was developed by Tai et al., who used in-situ TEM observation to describe the plasma process and presented the fabrication process of the TEM plasma microcell (***Fig. 1.7***).[26]

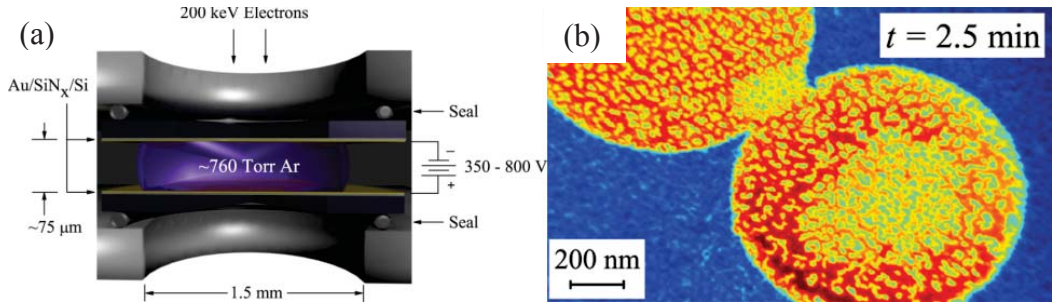

Fig. 1.7 *In-situ TEM observation for plasma processing(a) cross section of in-situ TEM plasma microcell developed by Tai et al.;* [26] *(b) false-color TEM image of plasma microcell anode surface after 2.5min plasma process, island (in yellow color) formation was observed; Credit to Tai et al.* Sci Rep 2013;3:1325 ©2013

The microcell was fabricated using TEM grids with silicon nitride window (purchased from Ted Pella®) and polymer balls with 1µm diameter were used to shade the Au deposition and result some observation area (***Fig. 1.8***). [26]

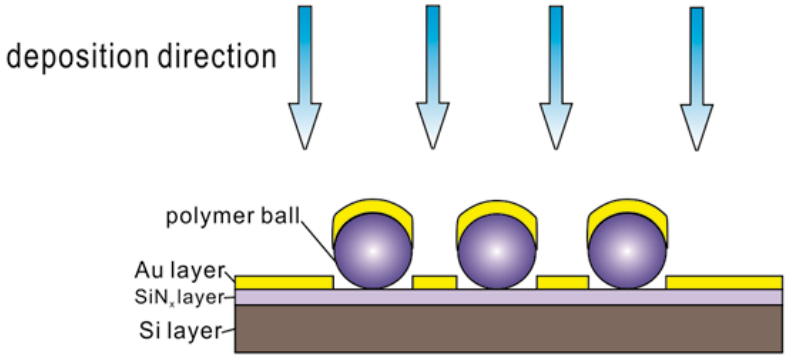

Fig.1.8 *Polymer ball masking illustration: polymer balls are used as mask and they can be easily removed by organic solvent*

The Au-coated area on the silicon nitride window acts as both anode and cathode in plasma generation.[26] Such prepared plasma electrodes were sealed face to face by using polymer O-rings to form a microcell (***Fig. 1.7(a)***).[26] The enclose Ar gas was sealed inside the microcell inside a glove box at 1atm pressure. The ionized Ar atoms act as the source of bombardment in the subsequent plasma experiments.[26] Furthermore, the purple color plasma image was captured ex-situ by using an optical microscope equipped with a CCD camera to show the generation of plasma. In this work, both etching and deposition

characteristics were characterized by in-situ TEM observation.[26] The sputter of Au particle on Au-coated cathode was proven by the timelapse video captured by TEM. According to real time image recording, the sputtering rate of Au film was measured to be 1.2×10^{-2} nm/s at 400VDC and 28mW power that was applied via an external power supply.[26] In addition, the deposition of Au particle on an uncoated area on the anode was characterized. Under 700VDC and 80mW power, Au deposited on the anode formed islands when it reached a critical thickness value and this kinetic was found to follow the Stranski-Krastanov growth mode, also known as "layer plus island growth" (***Fig.1.9***).[26]

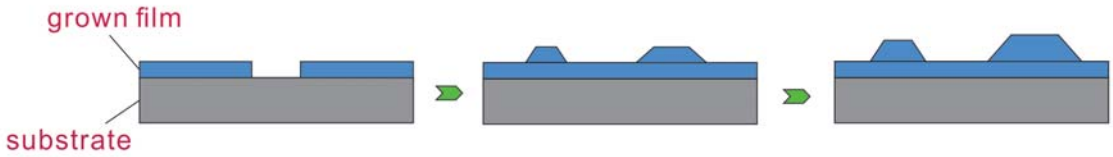

Fig.1.9 Stranski-Krastanov growth mode: when film thickness reaches some critical value H_c, island growth will begin

The growth rate of Au islands is dependent on the plasma power and can be related to DC sputtering diode model proposed by Stutzin et al. (***Fig.1.10***) [27]:

$$R = \frac{P_d\{x_{th}\}}{G\rho(1+\gamma)E_s q}$$

where P_d is power density of discharge, $\{X_{th}\}$ is the mean thermalization distance for an atom, G is the inter-electrodes gap distance, ρ is the atomic number density of deposited Au film, γ is the secondary electron emission coefficient, E_s is the average sputtering energy for Au and q is the unit charge. The preferential etching was also observed starting from contaminant landing sites and developing outward.[26]

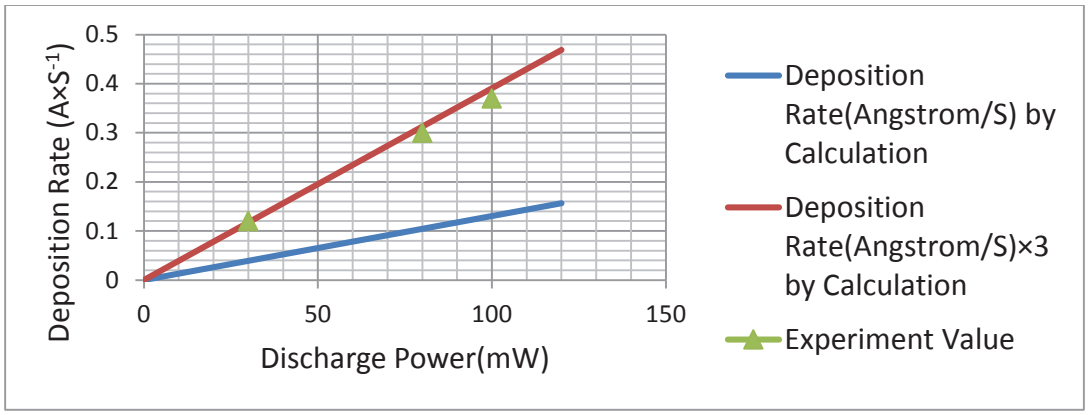

Fig. 1.10 *Au island growth rate plotted as a function of discharge power compare to the growth rate predicted by DC sputtering diode model* [26]*;*

However, the imaging resolution of 100nm limited subnanometer analysis of the in situ deposition and etching phenomenon. Due to the large electrodes gap distance (75μm) used, a larger chance of electron scattering and lower the imaging quality are induced (***Fig. 1.7(b)***). Furthermore, because each microcell chip can only be used for one experiment, a shorter routine to fabricate plasma chips must be developed to prepare them consistently and inexpensively.

1.5. Order of chapters in this report

In order to perform in-situ TEM observation for plasma process a plasma chip needs to be fabricated. Therefore, it is important to review the design concepts related to plasma generation in micron size scales. In Chapter 2, plasma generation criteria and the Paschen's law are introduced. Paschen's law is the governing law for plasma ignition and it gives the relationship between breakdown voltage and the gap distance. Paschen's curve was used to determine the gap distance of the plasma chip and predict the breakdown voltage. In Chapter 2, the plasma sheath distance is also discussed. In plasma physics, the smallest space dimension the plasma can exists must be larger than the sheath distance of the plasma. The sheath distance calculation of argon plasma in one atmosphere pressure is also presented in this chapter.

Because silicon nitride thin film with thickness of 50nm is used to form the plasma observation window and the plasma chip will be operating in a TEM high vacuum chamber, one the major concern is the mechanical strength of the thin film structure. In Chapter 3, the mechanical verification of chip that was done by performing a COMSOL simulation is discussed, including modeling and meshing steps.

After the design and verification process, the plasma chip needs to be prepared by microfabrication. Therefore, the fabrication process of the plasma chip is described in Chapter 4. The lithography mask design and preparation, physical vapor deposition (PVD), and lithography pattern transfer are included in the discussed in Chapter 4.

An ex-situ plasma ignition experiment was done to check the functionality of the plasma chip. The experiment environment and plasma generation circuit setup is discussed in Chapter 5 and the breakdown voltage of the air plasma in the plasma chip is also reported in the chapter. After plasma process, the plasma chip was characterized by using SEM and EDS and the results are discussed in Chapter 6.

2. Design Principles of the Plasma Microcell Device

This chapter establishes the design principles for the TEM plasma chip. The microcell integrated in the plasma chip allows generation of plasma in a TEM chamber and high-resolution observation of materials processing under various plasma conditions. To allow high-resolution TEM observation, the plasma microcell should be as thin as possible to reduce the scattering of the TEM primary electron beams by silicon nitride thin films building the microcell and the gas enclosed.

However, the generation of plasma is governed by physical laws. Plasma is the ionized matter and can be influenced by external electromagnetic field as well as the magnetic field generated by itself.[28,29] Many ionized gases cannot be called plasma since they do not have collective behaviors like sheath shielding. [28] Thus, to design a plasma device, these theoretical design aspects need to be addressed. The breakdown voltage, gap distance between electrodes and enclosed gas pressure relationship is governed by the Paschen's curve. In plasma physics, the smallest special dimension of the enclosure should be larger than the sheath thickness (i.e. Debye length) to allow plasma existence. The sheath shielding is also one of the characteristic behaviors of plasma.[28]

2.1. The relation of plasma ignition voltage and distance between the electrodes

When a high electrical field is applied to neutral gas, free electrons contained will be accelerated immediately to very high speed because the electrons have low mass[1]. The accelerated electrons will move toward the anode. Because particle kinetic energy is related to its thermal energy, these fast electrons are called hot electrons.[28] In an environment full of cold gas molecules, hot electrons will be able to "knock out" the electrons in gas

molecule orbits through inelastic collision and thus ionize the gas molecule[1]. The ionization process schematic of Ar is given as an example (***Fig. 2.1***).

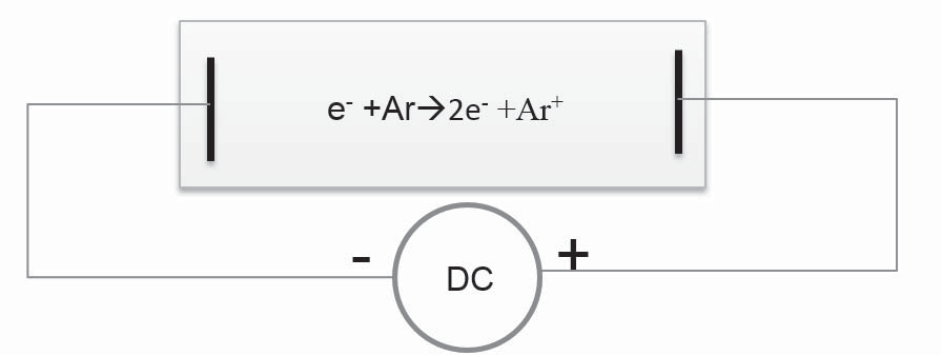

Fig. 2.1 *Gas molecules (e.g. Ar) can be ionized by high-energy electrons and this process also produces positive-charged ions and lower energy electrons*

The cascade ionization phenomenon will happen if the electrons generated from ionization still hold enough energy or can gain enough energy from the electric field to ionize more neutral particles. [30] The requirement for such breakdown to occur is governed by the Paschen's Curve[31]. The breakdown voltage, V_b, is given by:

$$V_b = \frac{BPd}{\ln(PdA) - \ln\left[\ln\left(\frac{1}{\gamma}+1\right)\right]} \qquad \text{(Equation 2.1)}$$

where the unit for A is $(\text{torr}\times\text{cm})^{-1}$ and B is in V/ (torr×cm). The parameters A and B are constants depending on the gas chemistry (See ***Table 2.1***). The parameter γ (unit less) is the Townsend second ionization coefficient for metals (see ***Table 2.2***), P is pressure in bar, and d is the distance between electrodes in cm.

Table.2.1 *Constants A((torr×cm)$^{-1}$)and B (V/ (torr×cm)) for different gases*[32]

gas	***A***	***B***
Air	14.6	365
Ar	13.6	235
H_2	5.0	130
He	2.8	34

Table.2.2 *Townsend second ionization coefficient (γ) for metals* [32]

gas / metal	**Air**	**Ar**	**H_2**	**He**	**N_2**
Al	*0.035*	*0.12*	*0.095*	*0.021*	*0.10*
Cu	*0.025*	*0.058*	*0.050*	_	*0.066*
Fe	*0.020*	*0.058*	*0.061*	*0.015*	*0.059*
Pt	*0.017*	*0.058*	*0.020*	*0.010*	*0.059*

Using ***Eq.2.1***, Matlab was used to plot the Paschen's curve, which predicts the air plasma ignition voltage in different gap distance between copper electrodes. Constant A=14.6 (torr×cm)$^{-1}$, B=365 V/(torr×cm), and γ=0.025 were measured by Cobine.[32] The outputs are plotted in log scale (***Fig. 2.2***). The Matlab code used is documented in Appendix 11.1.

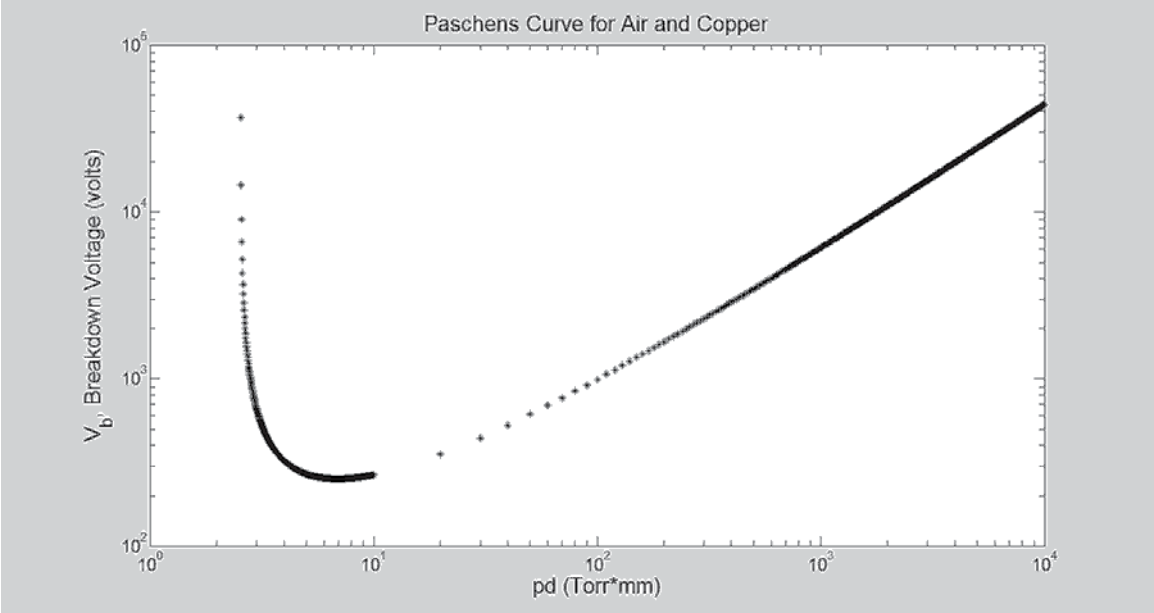

Fig.2.2 *The Paschen's curve for air with copper electrodes in log scale*

Note for convenient, the x-axis data in ***Fig.2.2*** are converted to torr×mm from torr×cm. The plotted Paschen's curve suggests that the minimum breakdown voltage of 252.4V can be reached at *Pd*=6.82 mm×torr, where *Pd* is the product of pressure *P* (torr) and gap distance *d* (mm) between parallel plate electrodes. Thus, in atmospheric pressure (760 torr), the minimum breakdown voltage can be reached at a distance of 8.9 μm between the electrodes.

2.2. Plasma Debye length calculation

In plasma physics, one criteria for the existence of plasma is that the smallest dimension of the space must be longer than the Debye length (λ_D) (see ***Fig.2.3***).[28] Debye length is one measure of plasma sheath thickness and it is also an important characteristic of the plasma collective behavior.[28] Thus, it is also important to estimate the Debye Length of the plasma under experimental condition.

The Debye Length, λ_D, can be calculated by using equation:

$$\lambda_D = \sqrt{\frac{\varepsilon_0 K T_e}{n_e e^2}} \qquad \text{(Equation 2.2)}$$

where ε_0 is the permittivity of free space (8.854×10^{-12} farad/m), K is Boltzmann's constant 1.38×10^{-23} joule/k, T_e is the electron temperature in °K, n_e is the number of free electrons and e is charge of proton 1.602×10^{-19} C [28]. Plugging in the above values, Equation 2.2 can be simplified to:

$$\lambda_D = 69.09\sqrt{\frac{T_e}{n_e}} \qquad \text{(Equation 2.3)}$$

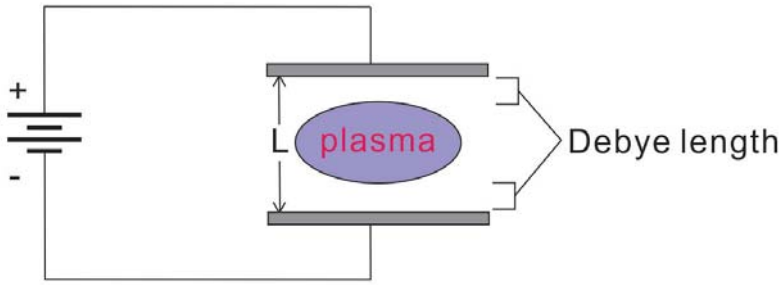

Fig.2.3 *Schematic of Debye length [28]: The regions close to walls appears darker compared to the bright plasma glow and this dark region is known as plasma sheath. The thickness of the plasma sheath is its Debye length.*

Assuming the room temperature is 300°*K*, the atom density N_a (the number of atoms in $1m^3$ volume) in Ar gas can be estimated by ideal-gas equation[33]:

$$\frac{n}{V} = \frac{P}{RT} \qquad \text{(Equation 2.4)}$$

where n is the atom number of a given gas in mol, P is the absolute pressure in Pa, V is the air volume in m^3 , R is the molar gas constant 8.31 J/mol×°K, and T is temperature in °K. Thus, by the definition, atom density N_a is given by:

$$N_a = \frac{n}{V} \cdot N_A = \frac{P \cdot N_A}{RT} \qquad \text{(Equation 2.5)}$$

where N_A is the Avagadro constant (6.02×10^{23} /mol).[33] From Equation 2.5, N_a is 4.816×10^{24} /m^3 in room temperature (300°K) and at 1 atm pressure, given 1 atm= 1×10^5 Pa. Because the first ionization energy of Ar is 15.76 eV [34], which is well above the range of cold plasma (1-10 eV), in cold plasma there can be only a small fraction of Ar ionized. According to the Vasenkov's work, the ionization ratio α is less than 10^{-6} in e-beam generated argon plasma gas flow. [35] So the electron density n_e can be determined by:

$$n_e = N_a \cdot \alpha \qquad \text{(Equation 2.6)}$$

Thus, the electron density in the cold plasma at 1 atm pressure is evaluated to be 2.41×10^{19} /m^3 by using Equation 2.5 and Equation 2.6:

$$N_a = \frac{n}{V} \cdot N_a = \frac{P}{RT} \cdot N_a = \frac{100000Pa \times 3.06\times10^{23} mole^{-1}}{8.31 mole \cdot J^{-1}K^{-1} \times 300K} = 2.41\times10^{25}\ \mathrm{m}^{-3}$$

$$n_e = N_a \cdot \alpha = 2.41\times10^{25} m^{-3} \times 10^{-6} = 2.41\times10^{19} m^{-3}$$

For electron temperature, because the cold plasma has a range of 1 to 10eV, both of the upper and lower boundaries of the cold plasma are evaluated. First, assuming the cold plasma electron temperature is 1eV, which is about 11000 k, the Debye Length of Ar plasma at 1 atm is 1.47 μm by using Equation 2.3:

$$\lambda_D = 69.09\sqrt{\frac{T_e}{n_e}} = 69.09 \times \sqrt{\frac{11000^\circ K}{2.41\times10^{19} m^{-3}}} = 1.47\times10^{-6} m$$

Similarly, the Debye Length of Ar plasma with 1eV electron temperature is evaluated at two other gas pressures 0.5 and 0.2 atm, and the Debye lengths were calculated to be 2.09 and 3.16μm respectively. Second, the Ar plasma with 10 eV electron temperature was also evaluated in 1 atm pressure environment. By using the same method, we find the Debye lengths for Ar plasma with 10 eV electron temperatures at 1, 0.5 and 0.2 atm gas pressures are 4.50, 6.48, and 10 μm, respectively. Comparing these results with the minimum distance for the electrodes (8.9 μm) derived from the Paschen's curve, we concluded that

the minimal gap distance (L) for the existence of plasma in the microcell should satisfy $L>>10$ μm according to the definition (***Fig 2.3***). [1,28]

In experiment, electrical insulation spacer was used to control the gap distance between two electrodes. Consider the Debye length of plasma (10 μm) and the availability of insulation spacer, the gap distance of 60 μm was chosen. The Paschen's curve also predicts that in parallel plate electrodes with a gap distance of 60 μm, the breakdown voltage for air is 570 V according to ***Fig.2.2***.

2.3. Literature review on primary e-beam and gas interactions

Many e-beam and gas interaction researches have been done in the operating voltage (1-30keV) and gas pressure (0-300Pa) range of Environmental Scanning Electron Microscope (ESEM) to optimize their imaging quality [36-39]. ESEMs allow characterization of insulators without such preparation by providing a low pressure ionized gas environment [38,39]. In these works, scattered cross-section was estimated using methods such as experimental techniques and Monte Carlo simulation. The ionization effect of ESEM e-beam can generate positive and negative ions in the gas environment and the ionized gas can conduct the exceeded electrons accumulated on insulator samples.[38] The in-elastic scattering is mainly responsible for the ionization effect [38].

In 1999, Mathieu introduced a method to experimentally determine the total scattering section (σ_T) by measure the e-beam current in gas environment (I) and in high vacuum environment (I_0). A factor m is defined as the average number of collisions per electron induced. Thus, in a given accelerating voltage V_a (kV) we have the following relationship between I and I_0:

$$I = I_0 e^{-m} \qquad \text{(Equation 2.7)}$$

By reading the beam current from ESEM, the value of *m* can be then evaluated at different pressures.

According to Danilatos,[40] the average number of collision can also be defined by:

$$m = \sigma_T PL / KT \qquad \text{(Equation 2.8)}$$

where σ_T (in m^2)is the scattering cross section for the gas in use, *P* is pressure in Pa, *L* is the working distance and in m, *T* is temperature in °K and and *K* is the Boltzman constant(1.38×10^{-23} J•°K^{-1}). [39] Thus, the total cross section σ_T can be evaluated at given accelerating voltage (***Fig 2.4***).

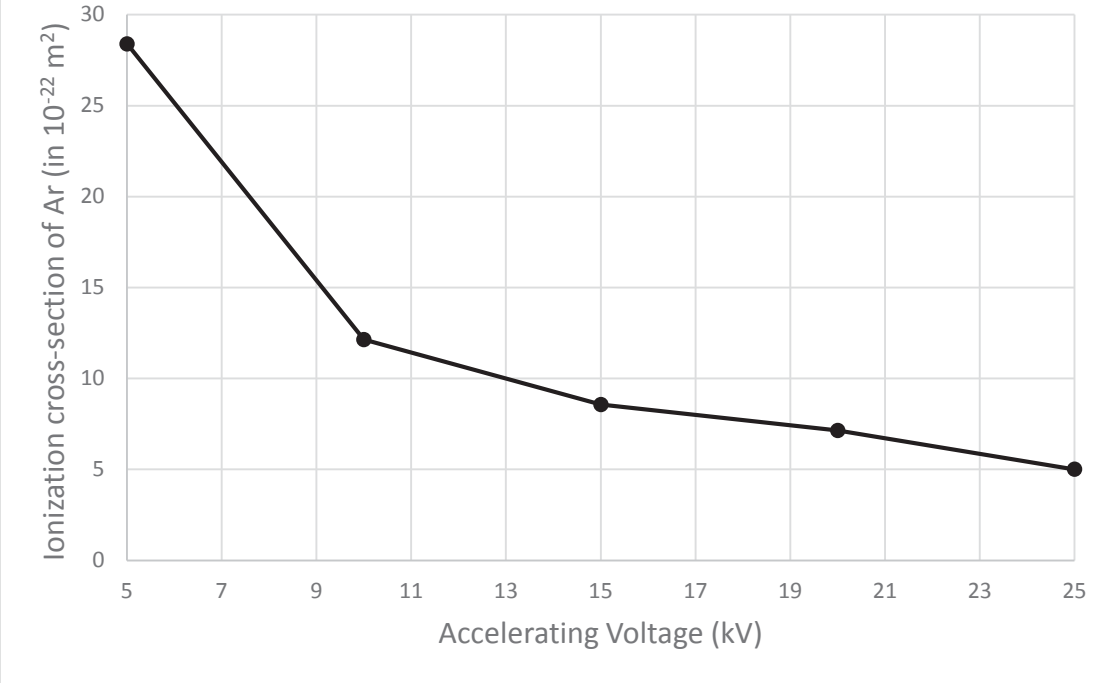

Fig.2.4 *Ionization cross-section area versus accelerating voltage for Ar gas in 1-100Pa range, data comes from Mathieu C., Scanning Microscopy Vol.13©1999* [39]

In 2003, Kadoun et al. adopted methods from Lenz[41] and Danilatos[42] and derived the total cross-section for Ar, N_2, and He gases in 0-50keV range. The cross-section of gases are derived by numerical integration of both elastic and inelastic differential cross-sections and according to Danilatos, the expression for atomic gas (Ar, He etc.) and molecular gas (N_2)

are different due to binding of atoms in molecular. As suggested by Kadoun et al. the differential cross-section for atomic gas with atomic number Z can be calculated by:

$$\frac{d\sigma_E}{d\Omega} = \frac{AZ}{16\left[\sin^2\left(\theta/2\right)+\sin^2\left(\theta_0/2\right)\right]^2} \quad \text{(elastic)} \quad \text{(Equation 2.9)}$$

$$\frac{d\sigma_i}{d\Omega} = \frac{A(\theta^2+\theta_E^2+\theta_0^2)}{(\theta^2+\theta_E^2)(\theta^2+\theta_E^2+\theta_0^2)^2} \quad \text{(inelastic)} \quad \text{(Equation 2.10)}$$

where

$$\theta_0 = \frac{\lambda}{2\pi R} \qquad \theta_E = \frac{J}{4E} \qquad A = \frac{\lambda^4 Z(1+\mathrm{E}/\mathrm{E}_0)^2}{4\pi^4 a_H^2}$$

λ is the electron wavelength defined by:

$$\lambda = 1.226\times10^{-9}\left[E\left(1+0.9778\times10^{-6}E\right)\right]^{-1/2}$$

and E is the energy of electron beam with unit eV. R is the atom radius, J is the ionization energy of the gas with unit eV, E_0=511,000eV is the rest electron energy and a_H is the Bohr radius which equals to 5.29×10^{-11} m.[36]

For molecular gases, the total scattering cross-section is affected by inter atoms biding in molecules. According to Danilatos [42], the differential cross-section for molecular gases may be derived by:

$$\frac{d\sigma_e}{d\Omega} = \sum_n \sum_j f_n(\theta) f_j(\theta) \frac{\sin(\mathrm{s}\times \mathrm{r}_{nj})}{\mathrm{s}\times \mathrm{r}_{nj}} \quad \text{(elastic)} \quad \text{(Equation 2.11)}$$

where $s = 4\pi\sin(\theta/2)/\lambda$ and r_{nj} is the distance between two atoms n and j. $f_n(\theta)$ is the function of scattering amplitude. The inelastic scatter cross-section for molecular gas is defined by:

$$\frac{d\sigma_i}{d\Omega} = \sum_j \frac{d\sigma_{ij}}{d\Omega} \quad \text{(inelastic)} \quad \text{(Equation 2.12)}$$

The total cross-section of He, Ae, and N_2 are calculated by numerical integration of Equation 2.15 through Equation2.18 (***Fig.2.5***).

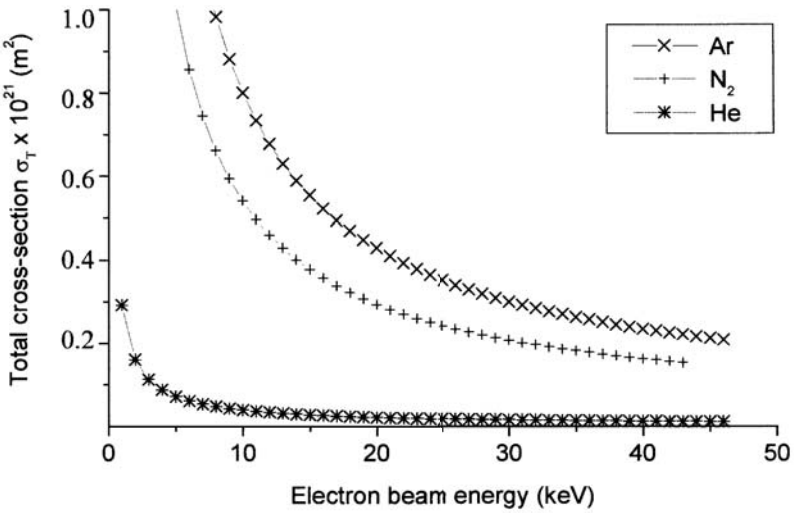

Fig.2.5 *Total cross section of Ar, He and N_2 gases versus e-beam energy[36]: figure reused under Creative Commons Attribution license. Kadoum A. et al. Vacuum vol.69 ©2003*

In 2012, Wight el al. constructed a dual Faraday cup (***Fig.2.6***) and integrated the device into environmental scanning electron microscope (ESEM) to measure scattered electron beam current (I).[43] The primary e-beam current (I_0) was measured under high vacuum.

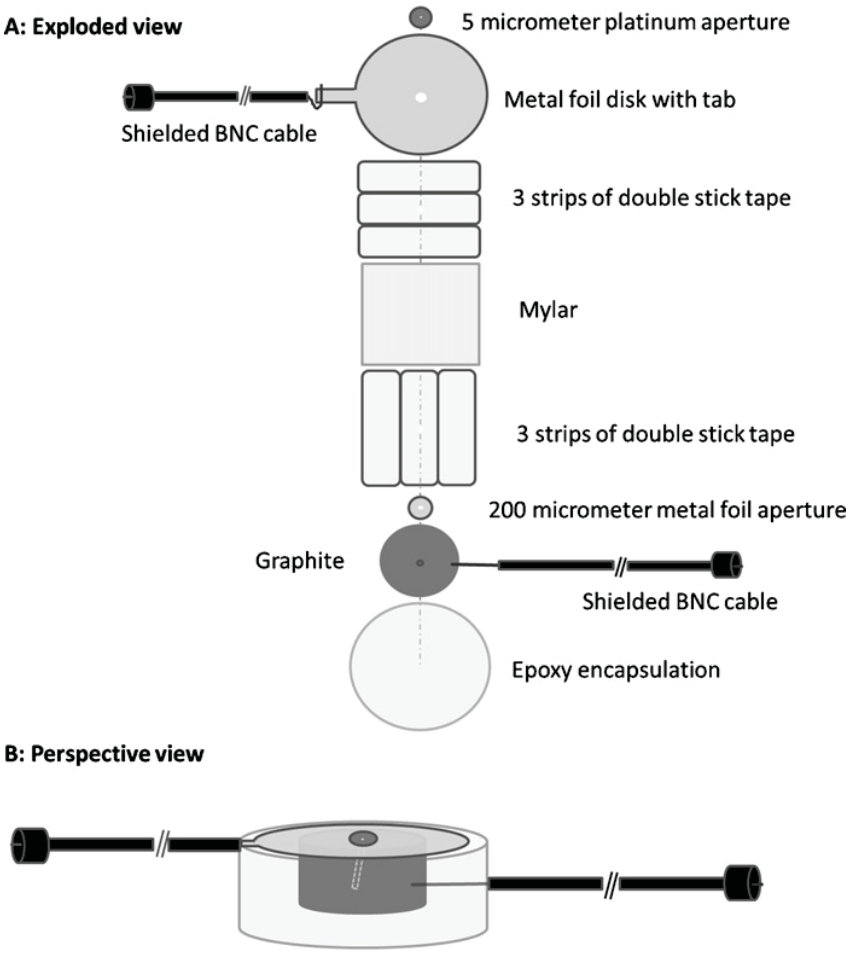

Fig.2.6 *The structure of Dual Faraday cup; A: exploded view B: perspective view*
Reprinted from Micro Vol.43, Wight S.A.et al. *Electron scattering cross section measurements in a variable pressure scanning electron microscope*, Pages 985, ©2012, with permission from Elsevier

By using Equation 2.13 and 2.14, the total scattering cross-section of water vapor, Ar and air were evaluated and plotted on 5-30keV range and the ionization potential for were taken both first ionization potential according to Danilatos[42] and the mean ionization potential as suggested by Mansour el al.[37](***Fig 2.7***). [43]

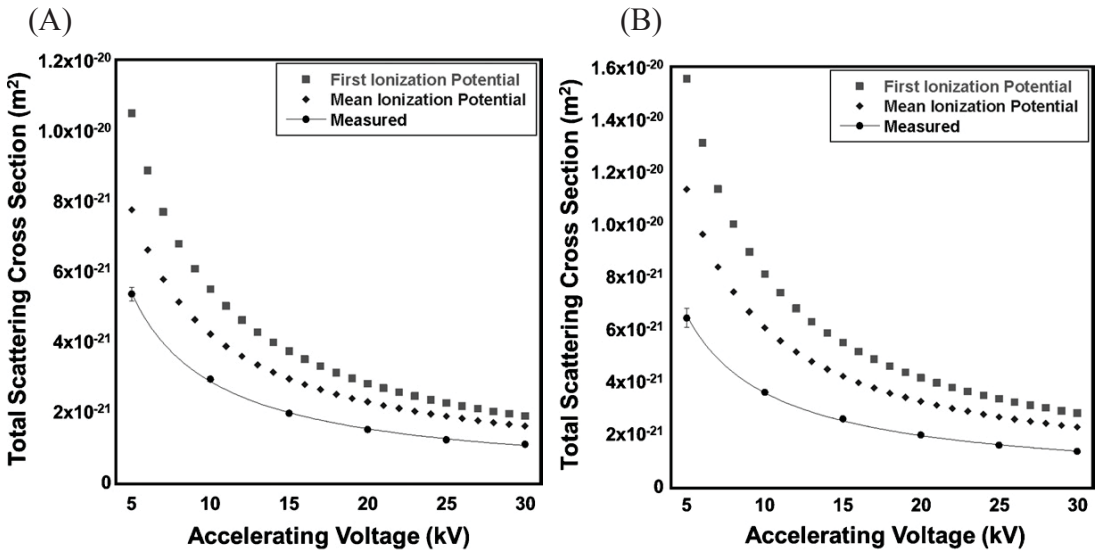

Fig. 2.7 *scattering cross section for Ar and air gas verses accelerating voltage (A) for Ar gas (B) for air. Error bar equals to one standard deviation*

Reprinted from Micro Vol.43, Wight S.A.et al. *Electron scattering cross section measurements in a variable pressure scanning electron microscope*, Pages 985, ©2012, with permission from Elsevier

Monte Carlo simulation is also used to e-beam scattering analysis. In 2010, Mansour et al. presented a work which employ Monte Carlo simulation to analyze low energy e-beam scattering in high-pressure scanning electron microscope. In computer based Monte Carlo simulation, random numbers (RND; 0<RND<1) were generated and the outcome of these random numbers were defined to represent an event happen or not.[37]

For electron collisions, the probability of the collision occur is p and when the random number RND>p then the collision event occurs. The probability of collision is defined by: $p = 1 - \exp\left[-L_p \sum \left(n\sigma_t(\mathrm{E})\right)\right]$ where $\sigma_t(\mathrm{E})$ is the total collision cross section. L_p is the average distance traveled by particles before a collision is happened (mean free path) and n is the atomic (or molecular) density of a gas. The value of L_p can be evaluated by: $L_p = 114.5(\frac{T}{M})^{\frac{1}{2}} \frac{\eta}{P}$ where T is the absolute pressure, M the molar mass of gas, η is the

viscosity of gas and P is the gas pressure.[37] Similarly, random numbers are also generated to determine whether a collision is elastic or in-elastic. The scattering angle can also be determined by a random number if the probability distribution of the angles are given.

2.4. Monte Carlo simulation of e-beam scattering due to interactions with gas

To analyze the ionization effect of the TEM e-beam, Monte Carlo simulation was perform by two different software: Win Casino3[44] and Win X-ray[45]. In the Win X-ray simulation, the e-beam energy was set to 200keV and the target was set to be Ar. The Ar gas is considered as a diluted solid according to Mansour et al [37] and the density (ρ) of Ar gas in 1 atm pressure was calculated by ideal gas law:

$$\frac{n}{V} = \frac{P}{RT} \qquad \text{(Equation 2.13)}$$

where n is the atom number of a given gas in mol, P is the absolute pressure in Pa, V is the air volume in m^3 , R is the molar gas constant 8.31 J/mol×°K, and T is temperature in °K.

Because $n = \frac{m}{M}$, where m is mass and M is molar weight, so the density (ρ) of Ar gas can be derived from the following calculations:

$$\rho = \frac{m}{V} = \frac{MP}{RT} = \frac{39.95g/mol \times 1atm}{0.0821L \cdot atm/(\text{mol}\cdot\text{K}) \times 300^{\circ}K} = 1.62g/\text{L} \qquad \text{(Equation 2.14)}$$

The absorbed electrons depth distribution in Ar gas environment was plotted by Win X-ray (***Fig 2.8***):

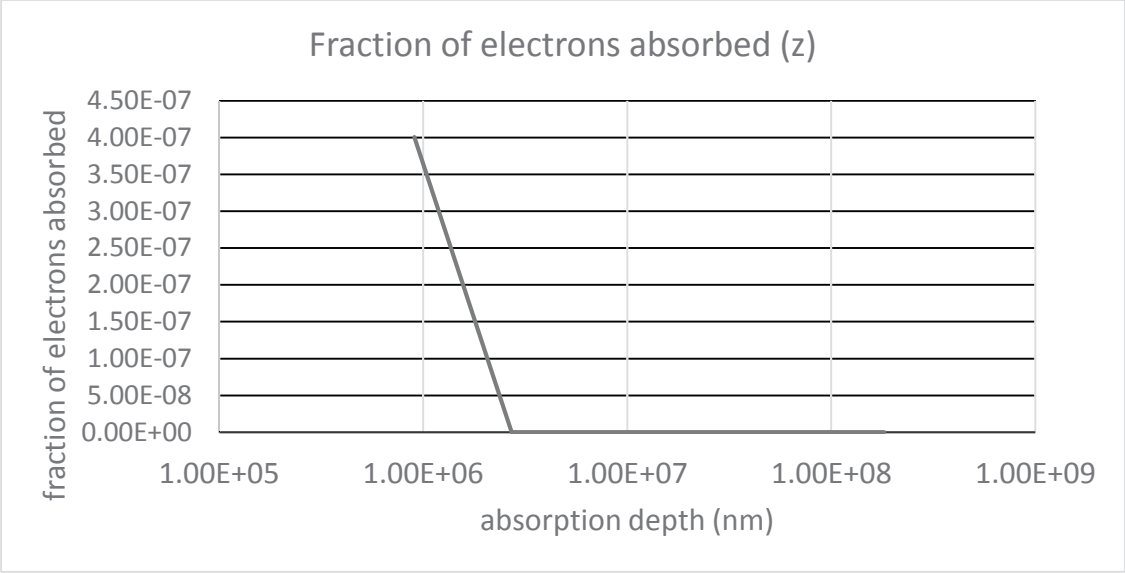

Fig. 2.8 *Win X-ray simulation of electron absorption: absorption depth distribution of 200keV electrons in 1atm Ar gas*

The Win X-ray electron absorption simulation result shows electron with 200keV energy will penetrate about 1mm (1×10^6 nm) Ar gas before being absorbed by other particles. The fraction of the electron being absorbed is about 4×10^{-7}.

A similar analysis was run on Win Casino3 as a comparison. The Ar gas layer was set to 60μm thick and 50nm silicon nitride layers were set on the top and bottom of the Ar gas according to the plasma chip design. The e-beam energy is set to 200keV and the Ar gas density is set to 1.62g/L as calculated before. The density of silicon nitride layer was set to 3.184g/cm^3 according to Shackelford el al. [46] The simulation result shows 95.3% of the electron transmitted from the plasma chip (***Fig.2.9***). The simulation results agree with Tai et al.'s work[26] that minor ionization will be induced by high energy TEM e-beam due to low scattering probability (<%4.7) and low electron absorption fraction (4×10^{-7}).

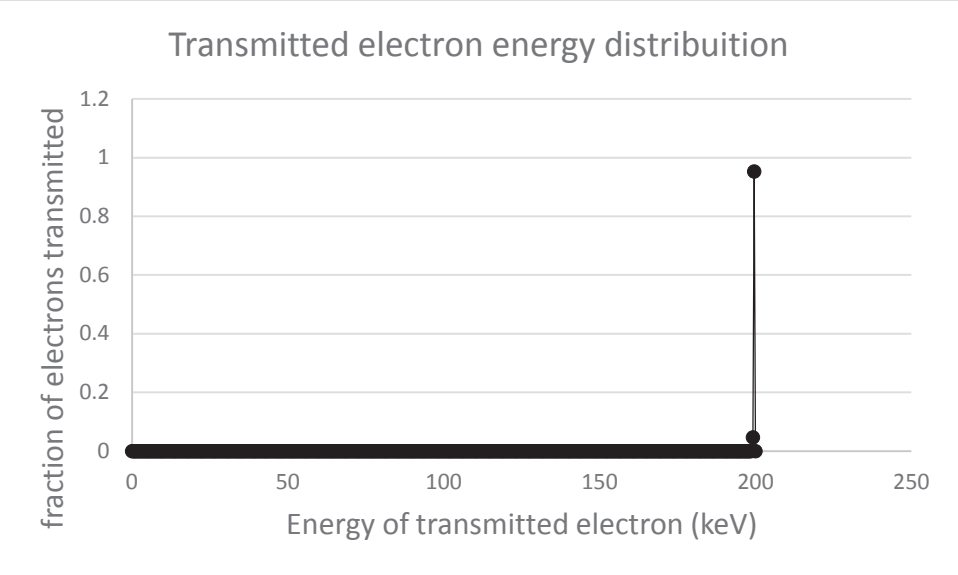

Fig. 2.9 *Win Casino 3 simulation of electron transmission energy distribution: 95.3% of electrons with 200keV energy transmitted in 60μm 1atm Ar gas layer with 50nm silicon nitride layers on the top and bottom of the Ar gas region*

2.5. Calculation on the effect of primary TEM e-beam on gas ionization

The primary e-beams generated by TEM have 200-400 keV energy depending on the accelerating voltage setting of electron microscopes. Such primary e-beams transmit through the plasma microchip to form the high-resolution images. During such transmission, the primary e-beam will interact with the gas atoms or molecules enclosed in the microcell and induce their ionization. As the mathematical derivations done by Dr. Alexei V. Saveliev at North Carolina State University, the e-beam and neutral particles interactions are discussed in this section.

The ionization rate $\dot{Q}_{ion}$ is given by:

$$\dot{Q}_{ion} = \frac{dn_{ep}}{dt} = \sigma \langle n_{eb} v_{eb} \rangle N \qquad \text{(Equation 2.15)}$$

where σ is ionization cross-section (about 10^{-16}cm^2) [47], $\langle n_{eb} v_{eb} \rangle$ is the flux of electrons in the electron beam and N is concentration of neutrals (at 1 atm N is about 3×10^{19} cm^{-3}).

The relationship between electron flux and electron beam current density is defined by:

$$j = \langle n_{eb} v_{eb} \rangle e \qquad \text{(Equation 2.16)}$$

By applying Equation 2.16, Equation 2.15 can be rewritten to:

$$\dot{Q}_{ion} = \frac{dn_{ep}}{dt} = \sigma \frac{j}{e} N \qquad \text{(Equation 2.17)}$$

Thus, by plug in constants given before, from Equation 2.17 we have:

$$\dot{Q}_{ion}\left(cm^{-3}s^{-1}\right) = 2\cdot10^{22}\, j\left(\frac{A}{cm^2}\right) \qquad \text{(Equation 2.18)}$$

Comparing with the quantity of the concentration of neutrals (3×10^{19} cm^{-3} at 1 atm), Dr. Saveliev concluded that within 1 ms, the major portion of neutrals will be ionized under the illumination of e-beam with current density of 10 to 100 μA/cm^2 and plasma will be ignited.

As introduced by Dr. Saveliev, the other effect induced by the incident high energy e-beam is the chemical dissociation. Silane (SiH_4) was given as an example. By assuming the dissociation cross section of silane is close to its ionization cross section, the dissociation rate of silane can be estimated by the following equation:

$$\frac{dN_{sd}}{dt} = \sigma \langle n_{eb} v_{eb} \rangle N_s \qquad \text{(Equation 2.19)}$$

The characteristic frequency of dissociation is given by:

$$\nu_d\left(s^{-1}\right) = \frac{dN_{sd}}{N_s dt} = \sigma \langle n_{eb} v_{eb} \rangle \approx 600 \cdot j(A/cm^2) \qquad \text{(Equation 2.20)}$$

By Equation 2.20, we can predict that with a current density of about 1 A/cm^2, the majority of silane molecules in the cell can be dissociated with a characteristic time of 1ms.

Nevertheless, the true nature of electron beam interaction with plasma gas is a matter of debate. Contradicting to the above calculations, others have shown that the primary e-beams have minor influence in ionization of the plasma gas since little electron inelastic scattering happens when high energy primary electron beam go through microcells with the thickness of 0.1-75 μm [25,26]. In Tai *et al.*'s work, Electron Flight Simulator® was used to simulate TEM e-beam with 200keV penetrating 1 atm pressure Ar gas.[26] The simulation results suggested that 3% of incident electron were inelastically scattered and 10^{-8} share of Ar atom were ionized due to the e-beam in a 75μm thick microcell. In the Sun *et al.*'s work, the same method was used to predict the ionization induced by 200 keV e-beam.[25] The results showed that 0.02% of e-beam electrons were inelastically scattered and the ionization rate induced by e-beam was evaluated to be 2.1×10^{-7} -1.9×10^{-6} $mol\times cm^{-2}\times s^{-1}$ in 100 nm thick microcell. But because the lifetime of ions is hard to predict, it is difficult to estimate the concentration of ion and electrons in the environment.[25]

Overall, because there is no detailed simulation and experimental work dedicated to the study of gas ionization by TEM primary electron beams, it is difficult to conclude whither high energy TEM electron beam can contribute significantly to the generation of plasma or not. So the author would like to bring the attention of researchers to the details study of such phenomenon in future tasks.

2.6. Chemical reactions induced by primary TEM e-beam

In an environmental cell that contains chemical species, high energy e-beam penetrates the cell and provides energy for both oxidation and reduction reactions (***Fig.2.10***).[26] Dr. Saveliev provided an example for silane (SiH_4) and Ar gas reaction under e-beam in TEM. Primary e-beam delivers its energy to Ar and SiH_4 by the following reactions:

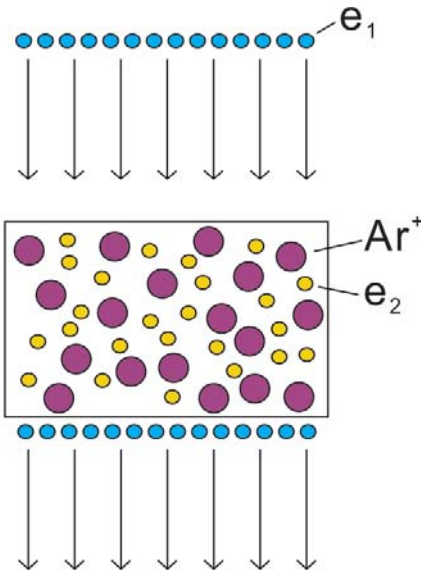

Fig.2.10 *TEM e-beam induced ionization: high energy electrons e_1 can ionize Ar atoms and escape or scattered and become lower energy electrons e_2 which can be captured by other chemical species*

$$Ar + e_1 \rightarrow Ar^+ + e_1 + e_2 \qquad \text{(Reaction 2.1)}$$

$$SiH_4 + e_1 \rightarrow SiH_3 + H + e_1 \qquad \text{(Reaction 2.2)}$$

where e_1 indicates high energy electrons (hot electrons) and e_2 indicates lower energy scattered electrons (cold electrons). Cold electrons can be then captured by neutral atoms. Molecules and ions may transfer their electrons to other chemical species by the following reactions:

$$Ar^+ + Ar + Ar \rightarrow Ar_2^+ + Ar \qquad \text{(Reaction 2.3)}$$

$$SiH_4 + Ar^+ \rightarrow SiH_4^+ + Ar \qquad \text{(Reaction 2.4)}$$

$$Ar_2^+ + e2 \rightarrow Ar + Ar \qquad \text{(Reaction 2.5)}$$

$$Ar^+ + e_2 \rightarrow (wall) \rightarrow Ar \qquad \text{(Reaction 2.6)}$$

The reactions may occur in an environmental cell (Reaction 2.3-2.5) or at the wall of a cell (Reaction 2.6). Other chemical reactions may also occur in the plasma condition:

$$SiH_4 + H \rightarrow SiH_3 + H_2 \qquad \text{(Reaction 2.7)}$$

3. Plasma Chip Mechanical Structure Design and COMSOL Validation

The plasma microcell is made of two silicon-based chips and is used to generate plasma in a high vacuum environment. This should allow in-situ TEM observation of materials under plasma processing. To allow TEM observation, the plasma microcell must meet the following criteria: (1) The observation area of plasma microcell must be transparent for TEM electron beam. (2) The environmental cell in the plasma microcell must be able to hold 1atm pressure. (3) The electric field and gap distance must be able to ignite plasma. (4) The electric field in the plasma microcell must be in the same direction with the TEM electric field (or in beam current direction).

The in-situ TEM plasma microcell (***Fig.3.1***) is developed to allow gas confinement in the high vacuum TEM chamber. The plasma will be ignited by using a strong electric field across the top and bottom chips. Each plasma microcell was constructed by using two identical silicon base chips (top and bottom chips) and the two chips were separated by a PVC insulating layer. The chips were prepared from commercially available Ted Pella® TEM silicon nitride windows with 50nm thick silicon nitride observation windows and 50μm silicon substrate. On each chip, a 50nm Cu layer was grown on the top of the silicon nitride layer to form electrode and provide reliable electrical connection for the following experiments[48]. There are seven layers in the plasma microcell. In each chip, there are layers of 200 μm silicon, 50 nm silicon nitride, 50 nm copper, and 60 μm insulating spacer ring in the middle of the sandwiched structure (***Fig.3.2***). The thickness of the insulating spacer is determined by the Paschen's curve and other physical considerations as introduced in Chapter 2.

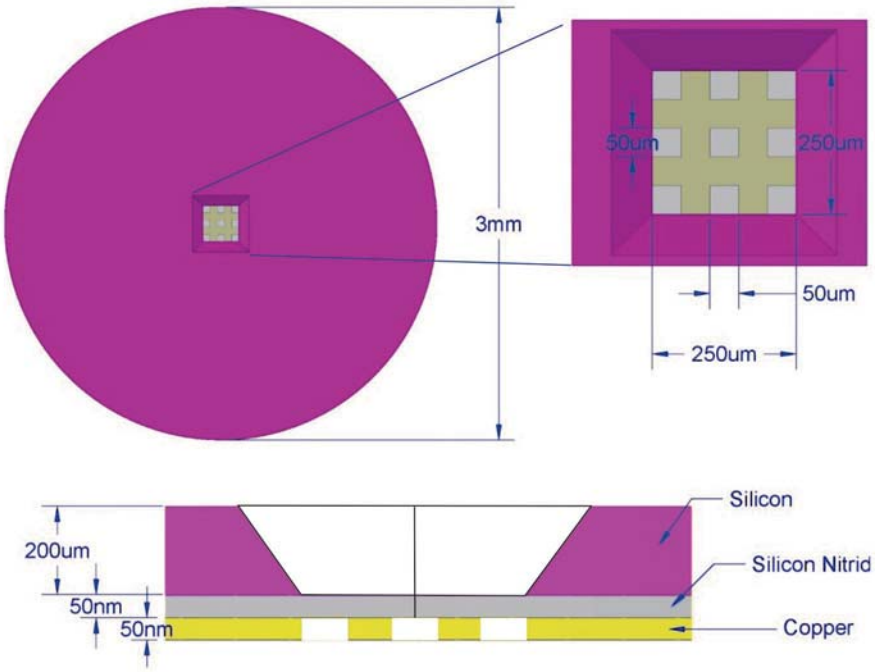

Fig. 3.1 *3D AutoCAD® design of the TEM plasma chip: silicon substrate is in purple, silicon nitride layer is in gray and copper layer is in yellow color.*

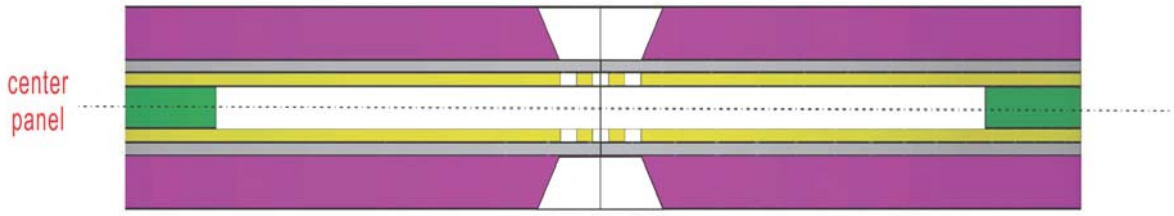

Fig.3.2 *TEM plasma microcell layer structure (section view): layer material from top to bottom: silicon (purple), silicon nitride (gray), copper (yellow), PVC spacer (green), copper (yellow), silicon nitride (gray), silicon (purple)*

3.1. Silicon nitride TEM window

To conduct the in-situ TEM experiment, the observation window must be covered by a material that is transparent to the TEM electron beam. Silicon nitride thin film has good transparency for a TEM electron beam, because it has lower scattering cross section[32]. As derived by using the Monte Carlo simulation in Chapter 2, less than 4.7% of primary electrons were scattered in 200keV TEM. Thus, silicon nitride thin film is good for observation window application. The silicon nitride layer should be deposited onto the silicon substrate and then the silicon substrate is etched away to allow the TEM electron beam to go through the silicon nitride window.

Because the silicon nitride thin film can be subjected to 1 atm pressure in the high vacuum TEM chamber, the film should be strong enough to hold the pressure. Low stress silicon nitride thin film grown by low pressure chemical vapor deposition (LPCVD) was chosen as the observation window material because it has a denser structure and stronger mechanical property than PECVD silicon nitride film[25]. Silicon nitride is also easy to integrate into the standard nanofabrication process for producing TEM plasma microcell with uniform quality.

3.2. Electrodes

Through the electrodes of the TEM plasma microcell, one can apply a strong electric field to the enclosed gas to induce gas ionization. The electrodes will act as plasma bombardment targets. Copper is used in this work as electrode material because it is widely used as the interconnection material in the semiconductor industry.

The copper thin film will be deposited directly on the silicon nitride layer and Direct Current (DC) sputtering deposition will be used for the process because of its good step-coverage. However, the deposition process will cover the entire silicon nitride film and

block the path reserved for TEM electron beam so an opening must be made at the nitride observation area to allow TEM observation (***Fig 3.1***).

3.3. COMSOL modeling

To verify the mechanical strength of the silicon nitride thin film to be used in the pressurized experiment, a model of the plasma microcell was built in COMSOL Multi-Physics®. Tetrahedral elements were used for dividing the model to exam the internal stress of copper and silicon nitride thin film structure under 760 torr pressure applied on one side.

Because the plasma microcell is symmetric with respect to the center panel (***Fig 3.2***), both electrodes of the plasma microcell experience equal force in opposite directions from the enclosed gas. For simplicity, only half of the microcell was simulated. The model was built according to the structure of the chip (half of the microcell), but it has a smaller cylindrical silicon substrate with 600 μm diameter and 200 μm thickness. In the center of the silicon substrate, a square opening was made by subtracting a cuboid 250μm×250μm×50μm by Boolean operation (***Fig. 3.3***).

A silicon nitride layer with 1mm diameter and 50 nm thickness was set on top of the silicon substrate and covered the square opening. Similarly, a copper layer with the same dimension as the silicon nitride layer was set on top of the silicon nitride layer. The properties of the silicon nitride layer such as Young's modulus (E=295 GPa) and Poisson's ratio (ν=0.23) are modified according to the Kaushik's work [49].

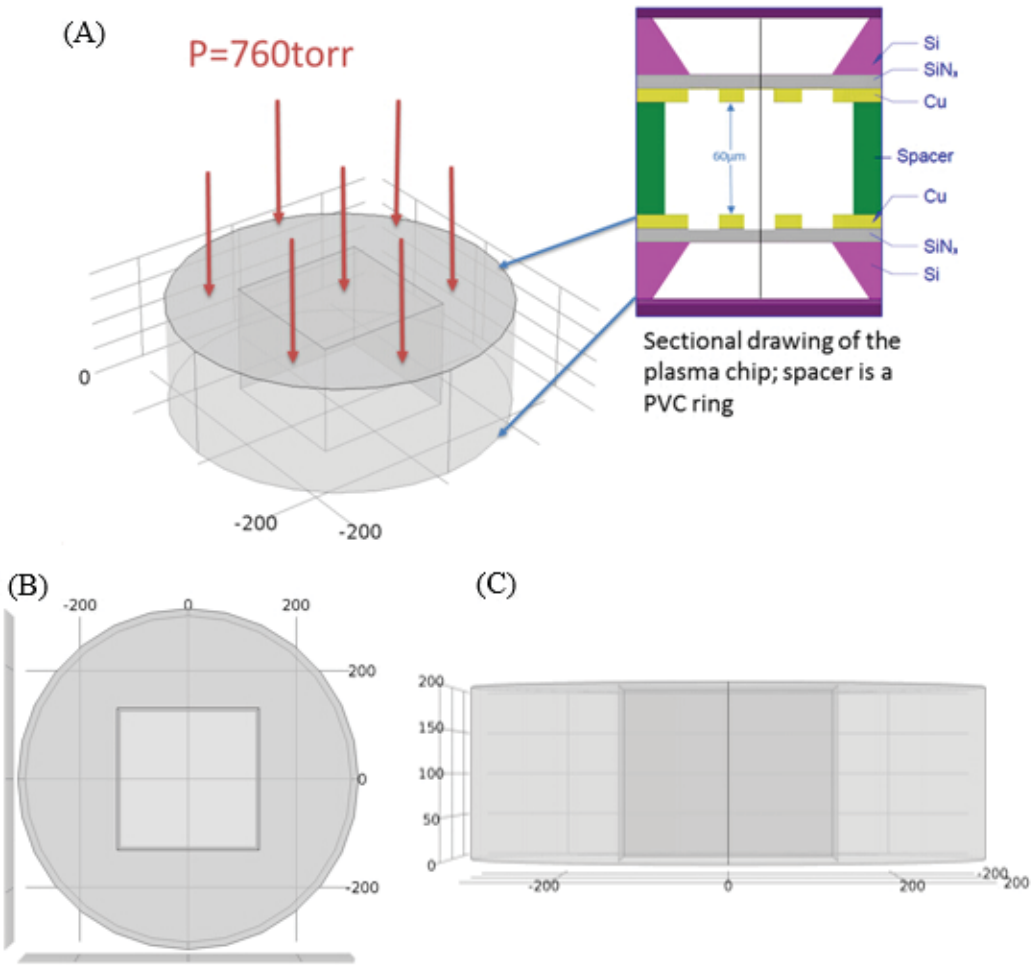

Fig.3.3 *COMSOL silicon nitride TEM window: the height of the model is 200μm silicon, 50nm silicon nitride and 50nm Cu (from bottom up). The radius is 300μm. Since the plasma microcell is symmetric about its center panel, only the bottom chip is simulated; the 760torr pressure was applied on the top of the electrode as shown in (A); (A) 3D view of the COMSOL model (B) top view of the model (C) side view of the model. The actual structure of the model was set according to physical dimension of the device as shown in* ***Fig.3.1***.

3.4. Model meshing

To increase the calculation accuracy and the simulation efficiency, tetrahedral elements with different sizes were used to mesh different layers and regions in the plasma microcell module. In the fragile copper and silicon nitride thin film window region, the tetrahedral elements sizes were decreased to improve calculation accuracy. In other regions, the tetrahedral sizes were increased to reduce calculation load. By doing this, the most accurate results can be generated at the most interested thin film region in an efficient computational time.

The mesh smoothness is governed by minimum element size, maximum element size, and element growth rate. The computer program uses different sizes of tetrahedral elements to divide the entire simulation model one and these three values give the upper boundary, lower boundary, and step increment of the tetrahedral size used. More time and computing power are need for smaller upper and lower boundaries, higher growth rates, and higher meshing quality.

In this work, 1μm minimum and 8μm maximum element sizes with 1.2 times maximum element growth rate were used to mesh the silicon nitride and the copper layers. A 5μm minimum and 30 μm maximum element sizes with 1.3 maximum element growth rate were used to mesh the bulk silicon substrate.

Because copper thin film will be etched from cathode and the thickness of the copper thin film is reduced during plasma process [26], two different models were built to simulate the plasma chip with and without the Cu thin film to represent the chip before and after the plasma process. It is also important to note that to mesh the high aspect ratio structure such that the x and y dimensions are much larger than the thickness (z dimension), a scale factor must be set to compensate the lower meshing quality in shorter dimensional axis before meshing. Tetrahedral meshing elements have the same length on its all six edges. Using them to mesh large aspect ratio structures, a single scale in all three dimensions results in

poor meshing quality in shorter dimensions and excessive meshing in longer dimensions. It is also important to know that a scale factor is only effective in the meshing step while using tetrahedral elements to divide the model. So it does not affect other computation steps and the final results.

In this work, the z axis dimension of the copper (50 nm) and silicon nitride layer (50nm) was only 100 nm, while the x and y dimension of the layer was 600 μm. A 1000 scale factor was set to z axis to make the software consider the z axis dimension of copper layer as 50 μm and silicon nitride thin film layer as 50 μm in the meshing step (***Fig.3.4***).

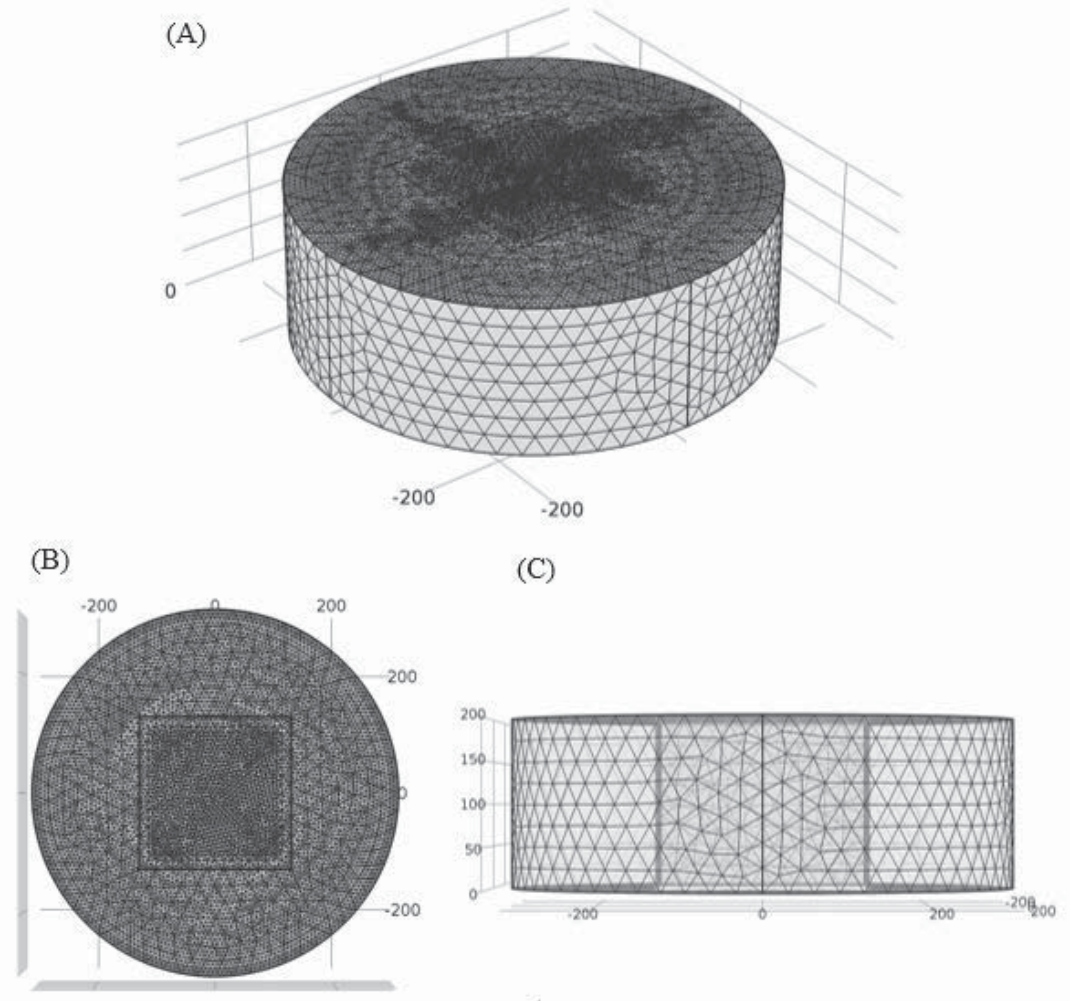

Fig.3.4 *Silicon nitride TEM window meshing: finer meshes was used on Cu and SiN_x thin film layer to improve simulation accuracy (A)3D view of the COMSOL model meshing (B)top view of the model meshing (c) side view of the model meshing*

3.5. Thin film stress analysis results

The Von Mises Stress and displacement were mapped for silicon structure. The stress distribution analysis result shows there is a maximum of 338.2 MPa internal stress built up in the thin film when 1atm pressure is applied on the top side of the electrode (***Fig.3.5***).

The maximum stress exists around the center of TEM window and on the center of each edge of silicon opening.

The total displacement analysis shows a maximum displacement of 94.4 nm is found at the center of thin film window when the 1atm pressure is applied (***Fig. 3.6***). It is not unexpected to see such a large deformation relative to thickness of the thin film (100nm in total). The X and Y dimension of the thin film covering the window is large (250μm×250μm) and the deformation of the thin film in the Z axis comes from the sum of the deformation in Z of every unit length of the thin film in X and Y dimension. Since the diagonal line of the square opening is $\sqrt{2}$ times longer than the edges, the strain of unit length of the thin film is lower than the edge and the stress on the diagonal line is lower than other place.

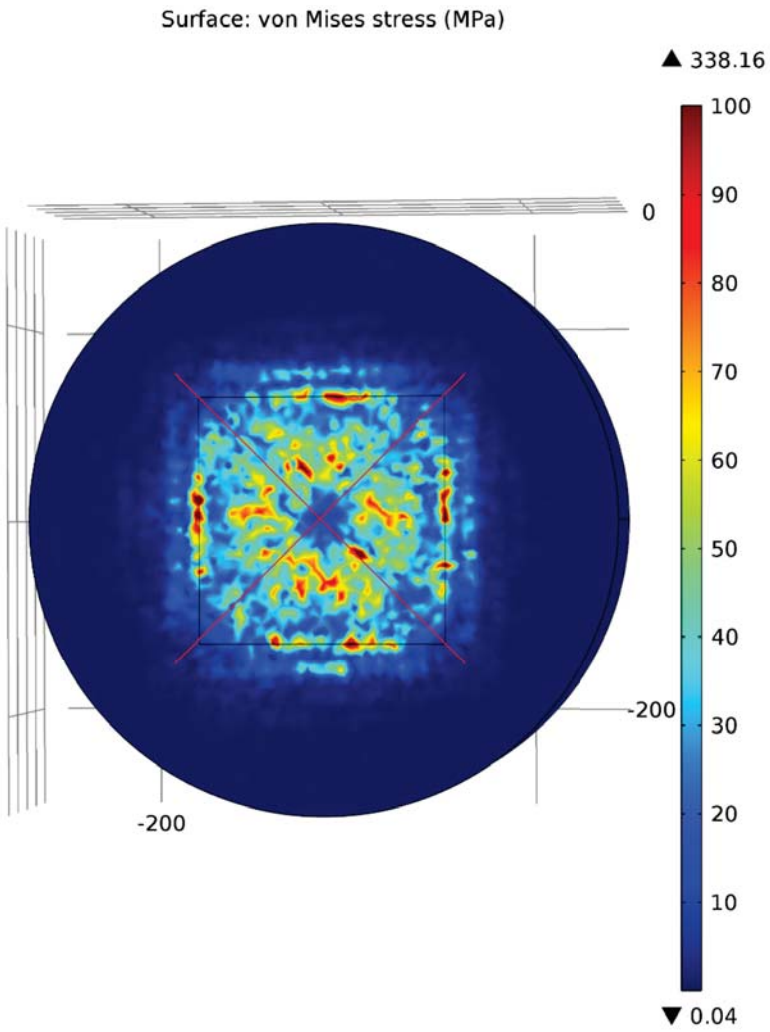

Fig.3.5 *Von Mises Stress mapping for in-situ TEM plasma chip with silicon nitride and copper thin film: the squire opening of 250μm×250μm on the silicon substrate induced the non-uniform structure of the stress and the stress on diagonal lines (red lines) is lower; stress over 100MPa is mark by red and stress below 10MPa is marked in dark blue.*

According to Kaushik's work, the burst strength for silicon nitride thin film is 7.1±0.2 GPa [49]. The simulation result suggests the maximum stress built up in the silicon nitride thin film is 338.16 MPa which is well below the bust strength. Thus, it is safe to use the 50nm thickness silicon nitride to build the in-situ TEM plasma micorcell in a high vacuum TEM chamber.

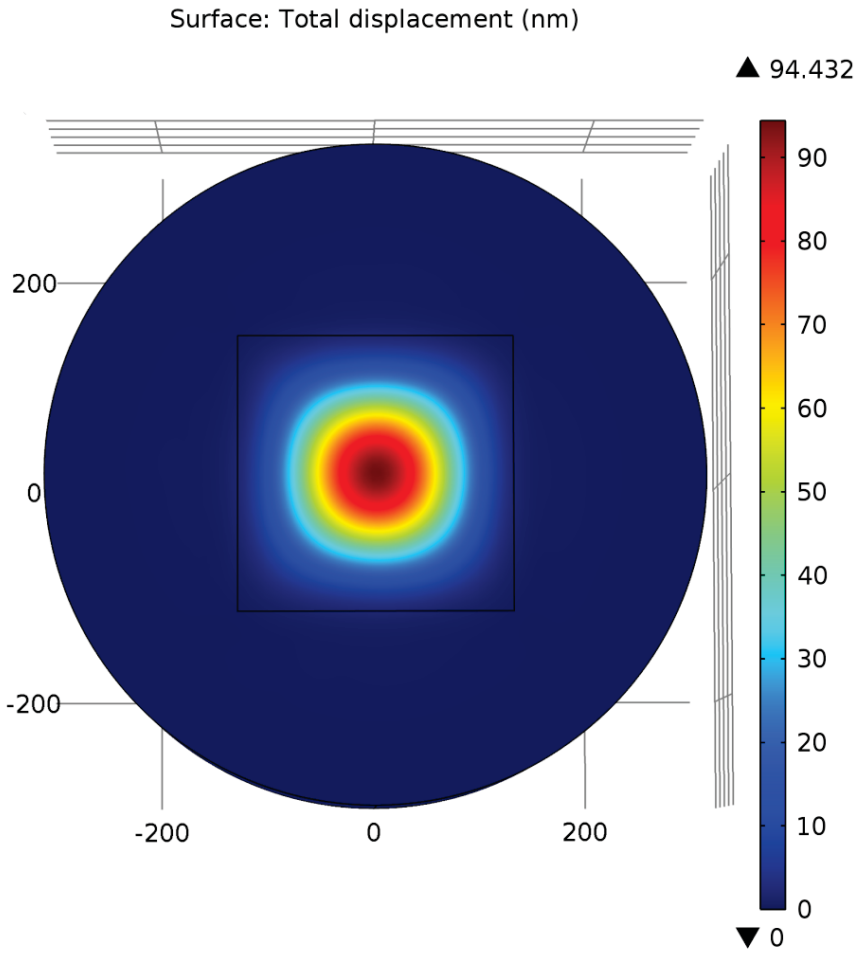

Fig.3.6 *Von Mises stress mapping for a microcell chip: both silicon nitride and copper thin film were considered. Deformation values more than 90 nm are marked in red and deformation less than 10nm is marked in blue.*

The simulation for the plasma microcell after plasma process (without Cu thin film) shows a gradual increase in the stress in the silicon nitride layer and a large deformation will result in less than 1 atm pressure (***Fig.3.7***). The maximum stress in the silicon nitride thin film increased to 988.98 MPa and the maximum deformation of the silicon nitride thin film increased to 113 nm (***Fig.3.8***).

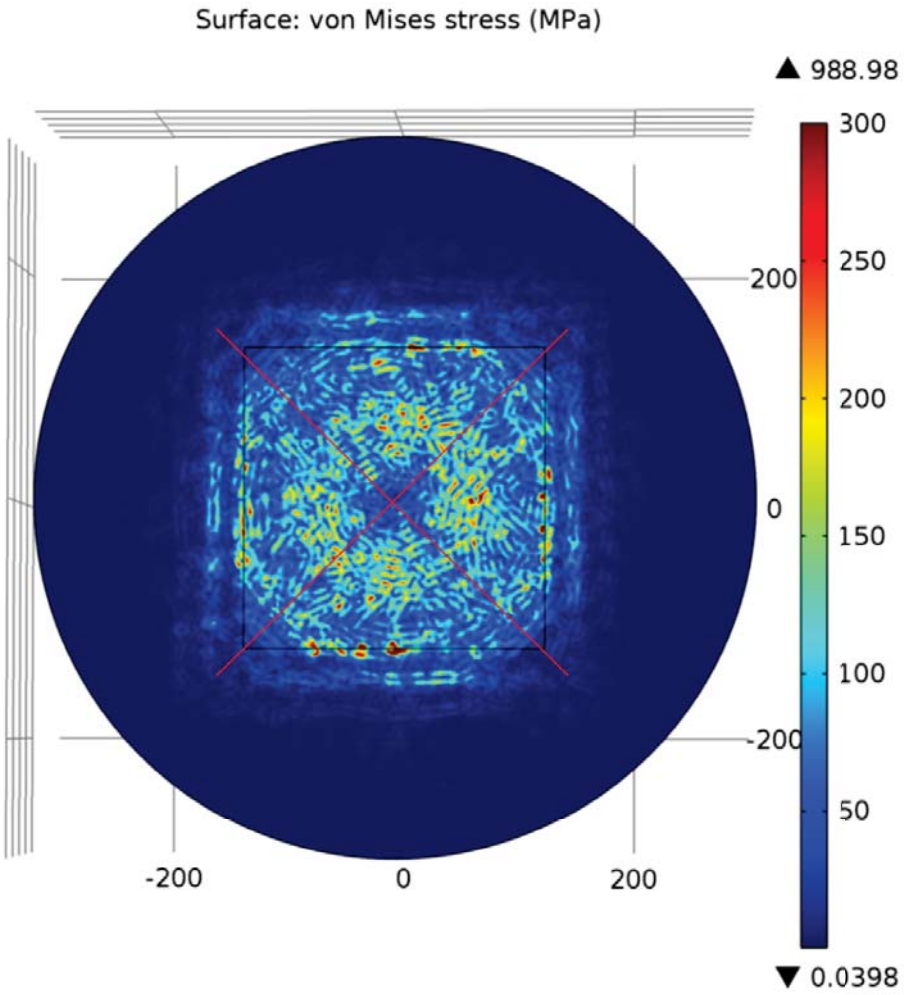

Fig.3.7 *Silicon nitride thin film stress distribution after Cu removal: stress over 300MPa is mark by red and stress below 50MPa is marked in dark blue. Red lines mark the lower stress region on the diagonal lines.*

Compare ***Fig.3.5*** and ***Fig.3.7***, we can see the maximum stresses in the silicon nitride thin film concentrate on the edges of the silicon opening and they remain the same before and after Cu thin film removal. This type of stress distribution agrees with typical clamped diaphragm stress distribution when pressure applied [50,51]. There is also a ring region around the center of the silicon window showing concentration of the stress. This indicates that this region experiences higher deformation. The diagonal lines region has lower stress since its longer length reduced the stress.

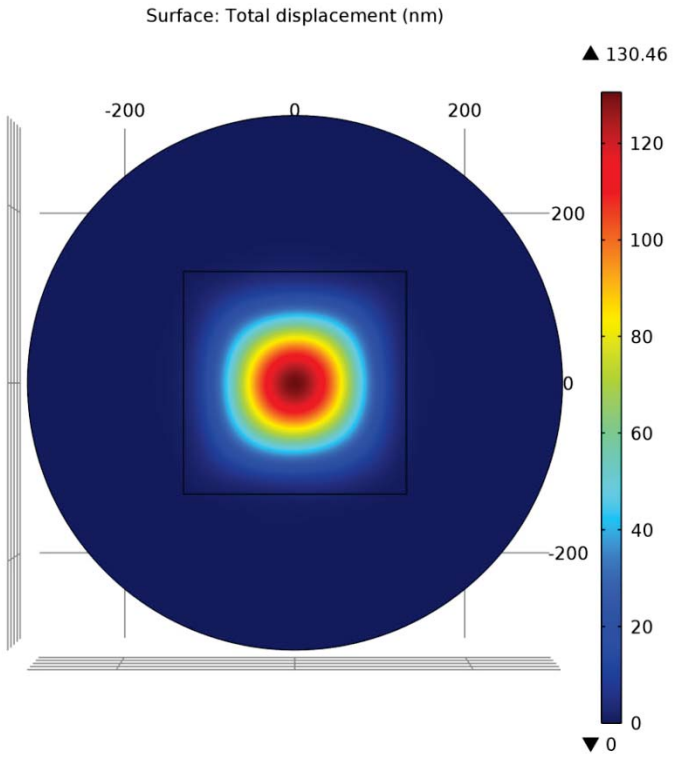

Fig.3.8 *Silicon nitride thin film deformation distribution after Cu being removed: the maximum deformation of 130.46nm is appeared in the center of the film*

The maximum stress distribution in silicon nitride before Cu thin film removal is 338.2 MPa stress under 1atm pressure. After Cu thin film removal, the maximum stress increases to 988.98 MPa, but both of these stress cases are much lower than the burst stress of silicon nitride thin film (7.1 ± 0.2 GPa) [49]. Considering the stress distribution in both models, we can conclude that the silicon nitride thin film is safe for sealing 1 atm gas in high vacuum environment. Thus, the physical structure design of the plasma microcell is considered to be appropriate.

4. Nanofabrication of the In-situ Plasma Chip Electrodes

The fabrication process starts from Ted Pella® silicon nitride window for TEM observation. The silicon nitride TEM window is a 3mm circular structure with 200μm thickness. The TEM window has a 200μm silicon substrate and coated with a 50nm low-stress silicon nitride layer on one side. The silicon substrate is etched through in the middle to form a 250μm×250μm TEM observation area so the observation area is only covered by the 50nm silicon nitride layer (***Fig. 4.1***).

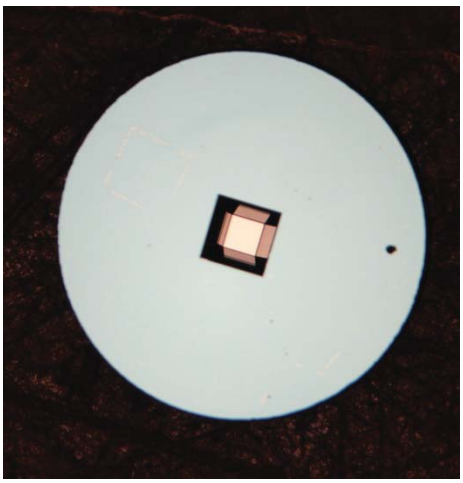

Fig.4.1 *Silicon nitride TEM window top view. The chips is fabricated by Ted Pella® and shows the silicon nitride TEM window with a center opening of 250μm×250 μm on silicon substrate. Photo taken by using an Olympus SZX12 zoom scope.*

The TEM plasma chip preparation experiment outline flowchart is shown in ***Fig 4.2***. The process flow is developed based on a "bottom up" sequence. The process starts from the Ted Pella® silicon nitride TEM window. A 50 nm Cu thin film was then deposited on the top of the silicon nitride thin film. Lithography pattern transfer was then used to make some observation windows in the Cu thin film layer. The fabricated plasma chips are then ready for bonding and plasma experiments.

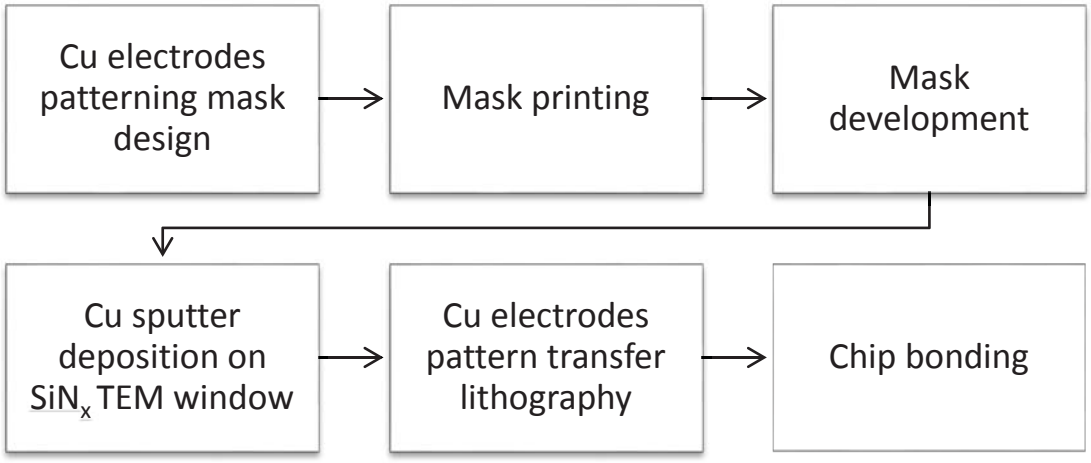

Fig.4.2 *TEM plasma chip fabrication flowchart*

The mask used for pattern transfer was first designed by using Auto CAD software. Then the mask was printed on a photoplotter film by a laser photoplotter (***Fig.4.3***). The printed film then need to be developed by using developer and fixer solutions before it can be used for lithography pattern transfer process.

4.1. Photolithography mask preparation

The clear field photolithography mask (***Fig. 4.4 (a)***) was designed using Auto CAD with 25μm minimum feature size. The mask (***Fig. 4.4 (b)***) was made in the Microfabrication Facility at Michigan Technological University by using a laser photoplotter. The operation was conducted under the direction and supervision of Jen-Yung Chang and Sterling Prince.

A laser photoplotter works like a printer. It use laser with 630-670 nm wave length to write on photoplotter films. The film was first cut into desired size and then taped onto the drum in the photoplotter (***Fig. 4.3***). The laser beam writes line by line onto the film with the movement of laser module and the rotation of the drum.

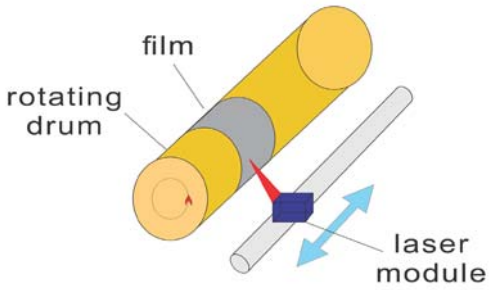

Fig. 4.3 *laser photo plotter operating schematic*

In this experiment, Kodak® ARPR7 photoplotter film was used. After printing, Kodak® Accumax Rapid Access Developer and Replenisher fixer were used for the mask making. Developer and fixer were mixed in 1:2 according to manufacture specification. The developer and fixer mixture were heated to 35°C and the printed film was dipped into the mixture for 45seconds. Then the developed film was dipped into DI water for 1min cleaning.

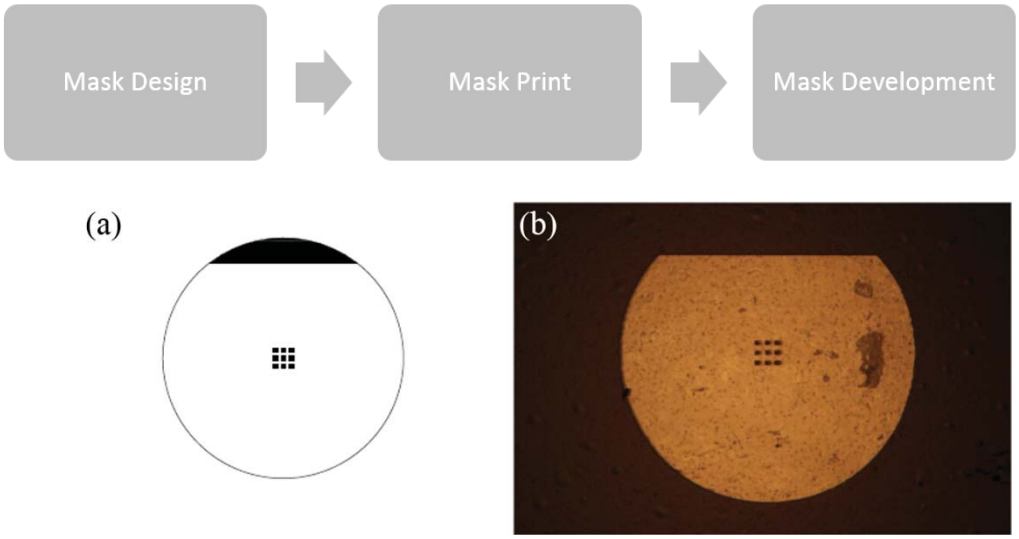

Fig.4.4 *Photo lithography mask for copper electrodes patterning (a) AutoCAD design of photo lithography mask (b) The prepared photo lithography mask, defect can be seen on the clear area*

In the clear field mask, the grid of rectangular shapes indicate the regions in Cu film that will be etched away (in cooperate with using negative tone photoresist). There are nine dark squares on the center of the mask representing the observation openings in the plasma chip. The designed photolithography mask has a dark region on the top of the plasma chip (***Fig.4.4*** *(a)*), which is used for electric isolation purpose. Unfortunately, defect (***Fig.4.4 (b)***) were found on the clear region of the developed mask. Because the defect was found in a random pattern, the defects may be originated from imperfect photoplotter film or the error of developer fixer mixture temperature control.

4.2. Copper deposition

New silicon chips with silicon nitride TEM windows (fabricated by Ted Pella®) were directly used for copper deposition without any clean process to avoid damage to the silicon nitride window. Silicon nitride windows were placed on pre-cleaned glass slide and loaded into the sputtering deposition system (***Fig.4.5***).

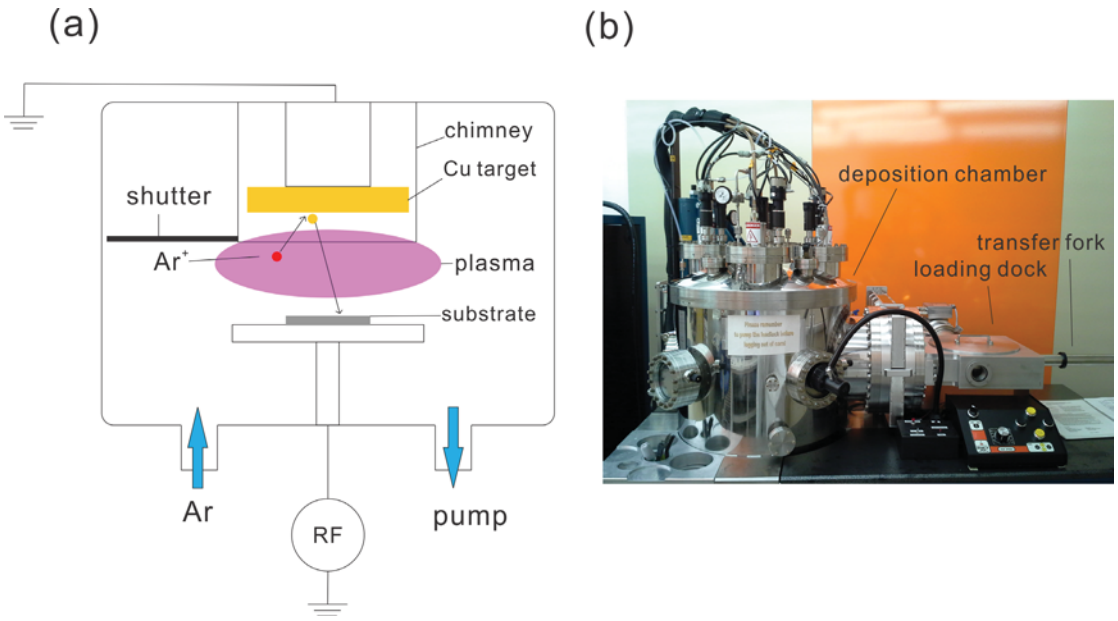

Fig. 4.5 *Sputtering deposition system (a) sputtering deposition operation schamemic (b) AJA sputtering deposition system in NFC at University of Minnsota*

The sputtering deposition system uses radio frequency (RF) power to ionize the enclosed Ar gas for plasma generation (***Fig.4.5 (A)***). The ionized Ar particles bombard the Cu target causing the removal of Cu atoms from target and their deposition onto the substrate. The AJA sputtering deposition system was located in Nanofabrication Center. It provides an automated shutter covering the plasma chimney. This device enables accurate time control of deposition process. When the shutter closes, the deposition stops immediately and when it opens, the deposition starts.

The loading dock attached on the deposition chamber is designed to maintain the clean condition in the deposition chamber. Any sample will be first loaded into the loading dock and will be kept there until the loading dock reaches to high vacuum. Then the sample will be transferred to the deposition chamber by using the transfer fork. The loading dock is separated from the deposition chamber by a mechanical valve.

A 50nm thickness copper layer (***Fig.4.6***) was deposited on the silicon nitride layer of the silicon nitride TEM window by using the AJA® sputtering system ATC2000. The chamber was first pumped down to 2.0×10^{-6} torr before loading the sample into the deposition chamber. The sample was then placed in the deposition chamber from the loading dock by using a transfer fork. Argon gas with 20sccm flow rate was used for plasma generation.

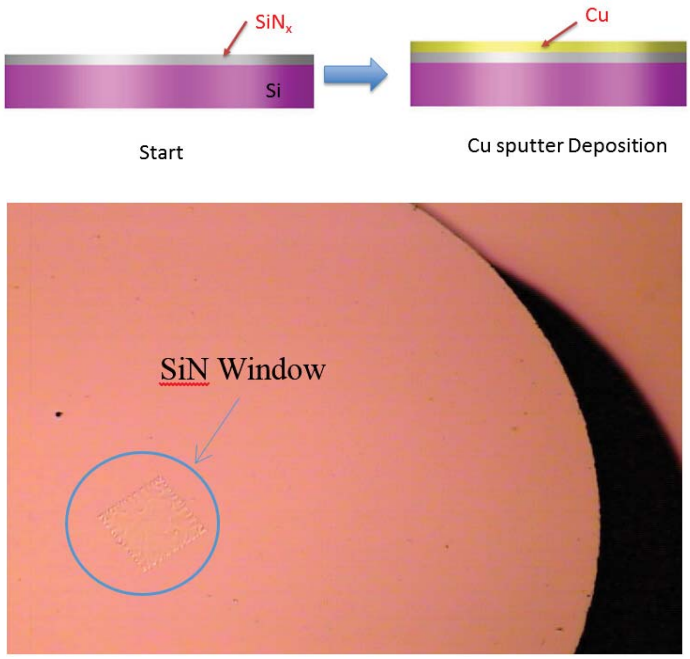

Fig.4.6 *50nm copper thin film deposited on top of silicon nitride TEM window, the silicon nitride window area appears brighter in color*

Before deposition, the copper target was first cleaned by Argon plasma for 2 mins at a power of 250 watts. The deposition operated for 110 sec to yield a 50 nm copper thin film on the top of silicon nitride layer. The deposition time was accurately controlled by a programmed shutter, which can cover the entire plasma chimney. The deposition rate was 275 Å/min, which was previously characterized by NFC staffs. The grown semi opaque copper thin film was then characterized by a VASE® ellipsometer (***Fig.4.7***). An average of 48.2 nm thickness of copper thin film was reported (***Table 4.1***).

An ellipsometer is a device that uses light polarization to determins material charactoristics including optical constants, film thickness, refrective index and surface roughness. The ligh polarization will change when beam light and surface interact with each other. The polarization data can be analyized to find interesting material charactoristics.

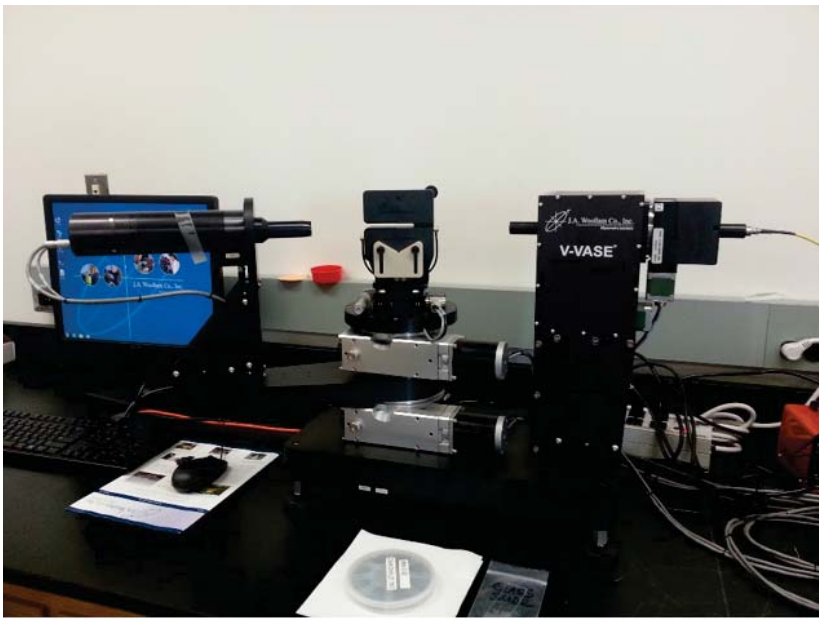

Fig.4.7 *VSAE® elllipsometer in Michigan Technological University*

Table.4.1 *Ellipsometer analysis result for copper thin film*

Sample Name	**First measurement (nm)**	**Second measurement (nm)**	**Average (nm)**
Sample 1	48.9	48.3	48.6
Sample 2	47.8	47.9	47.9
Average sample thickness	_	_	48.2

4.3. Electrodes patterning

The copper electrodes were patterned by photolithography process. Futurrex® NR71-1500P negative tone photoresist was used as both adhesive and wet etch mask. The lithography patterning process flow is shown in ***Fig 4.8***.

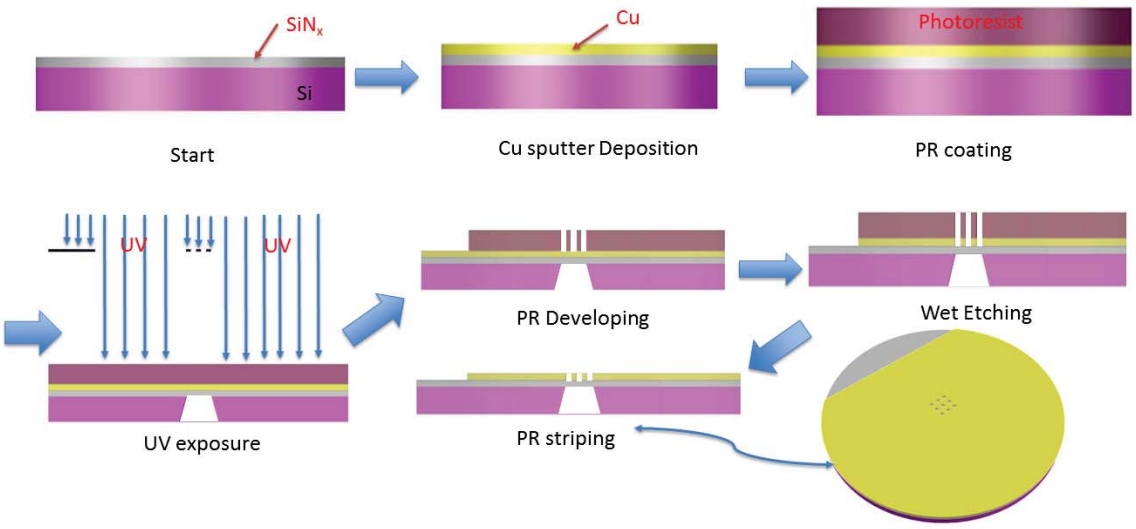

Fig.4.8 *copper electrodes pattern transfer fabrication process flow chart: silicon substrate is in purple, silicon nitride is in gray, Cu is in yellow, and photoresist layer is in purplish red.*

The fabrication steps involved in the Cu electrode patterning are outlined below:

Step 1*, Glass slide clean:*

A glass slide was first cleaned by acetone rinse for 1min and followed by 1min methanol rinse and this sequence is repeated for three times. Then rinse the glass slide with de-ionized water (DI water) for 3 mins. The slide was dried with nitrogen gas and then dehydrated using a hot plate to bake it for 5 min at 200ºC.

Step 2*, Adhesive coating:*

The glass slide was coated by NR71-1500P by spin coating with CEE200-X spin coater. The spinning program was set for 300rpm for 3s and followed by 3000rpm for 45s. This photoresist layer was act as adhesive for mounting the copper-coated Ted Pella® silicon nitride TEM window.

A spin coater has a rotating table where the substrate can be firmly mounted on it (***Fig.4.9***). The rotation speed can be controlled by computer. By rotating the substrate, the liquid

photoresist (PR) can be spread uniformly over the surface of the substrate. The thickness of the photoresist can be controlled by selecting different rotation speed. The faster the speed the thinner the PR film.

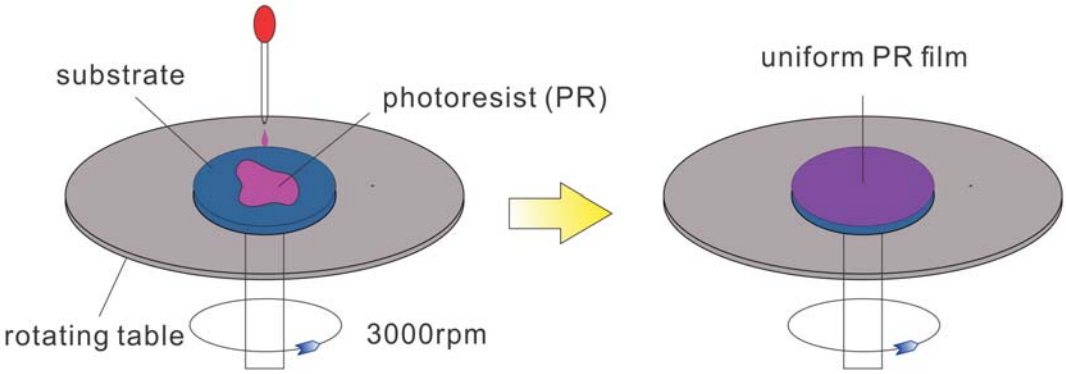

Fig.4.9 *Schematic of photoresist spin coating*

Step 3*, Sample mounting*:

Because there is no alignment mark on the silicon nitride TEM window produced by Ted Pella®, direct alignment between the window area pattern on the mask and the silicon nitride window was performed. The different color between the window area and its surrounding was employed to perform the alignment.

After photoresist coating, the copper-coated TEM window was loaded on the right side of the glass slide where it was aligned by a contact aligner. One edge of the silicon opening on the silicon nitride TEM window must be in parallel with the longer edge of the glass slide. Then the glass slide was soft-baked at 150ºC for 1.5 mins.

Step 4, *photoresist Coating:*

After soft baking, the glass slide was loaded in a hexamethyldislazane (HMDS) tank for vapor priming for 5 mins. This process removed water vapor on the surface of copper layer before photoresist coating. Then the glass slide was loaded to CEE200-X again for NR71-1500P coating by using the same program as in Step 2.

Step 5, *Alignment and Ultraviolet exposure:*

The glass slide and the sample was then softbaked on a hot plate at 150ºC for 2mins. After soft baking, the glass slide was transferred to a Karl Suss® MA6 contact mask aligner (***Fig.4.10***) for mask alignment and ultraviolet (UV) exposure.

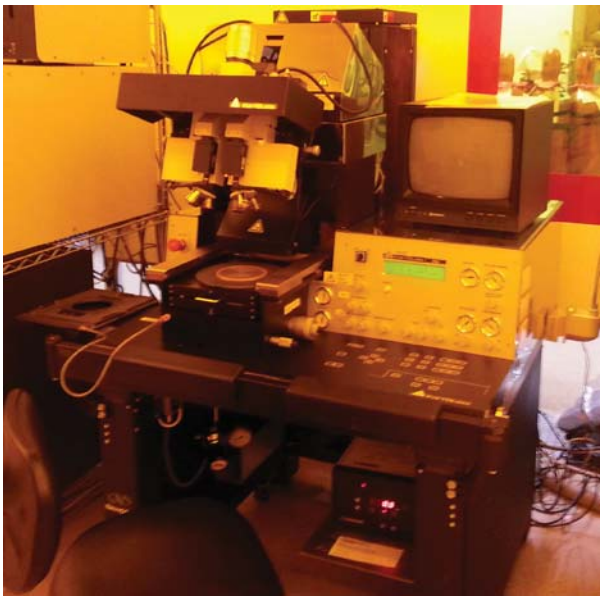

Fig.4.10 Karl Suss® MA6 contact mask aligner

The square opening array was aligned directly to the observation area of TEM silicon nitride window. Because the copper film is only 50nm, the silicon nitride observation area is visible under the microscope attached on the MA6 contact mask aligner. The exposure was completed in hard contact mode for 27 seconds and the wave length of 365nm was used for the exposure.

Step 6, *Post exposure bake and develop:*

The UV exposed sample was transferred to hot plate for post exposure baking for 2 mins at 100 ºC. Then the sample was developed by the RD6 photoresist developer for 18 seconds.

Step 7, *Wet etching:*

Fresh mixed copper etchant was prepared by mixing Citric Acid: Hydrogen Peroxide: Ammonium Hydroxide: DI water at a weight ratio of 2:1:1:96. The sample was immersed in the solution 45 seconds for wet etching. Then the sample was dropped into DI water for 5 mins rinse.

Step 8, *Photoresist strip:*

After wet etching, the sample was immersed in Photoresist Remover 1165 for 1hour to roughly remove the photoresist. Acetone, methanol, and DI water, were used in sequence to clean the sample for 3mins each after 1165 photoresist strip. Oxygen plasma cleaning system was then used to remove any photoresist residual remaining on the sample for 10 min. Subsequently, the TEM plasma electrode (***Fig.4.11***) was patterned and ready for mounting and wiring process.

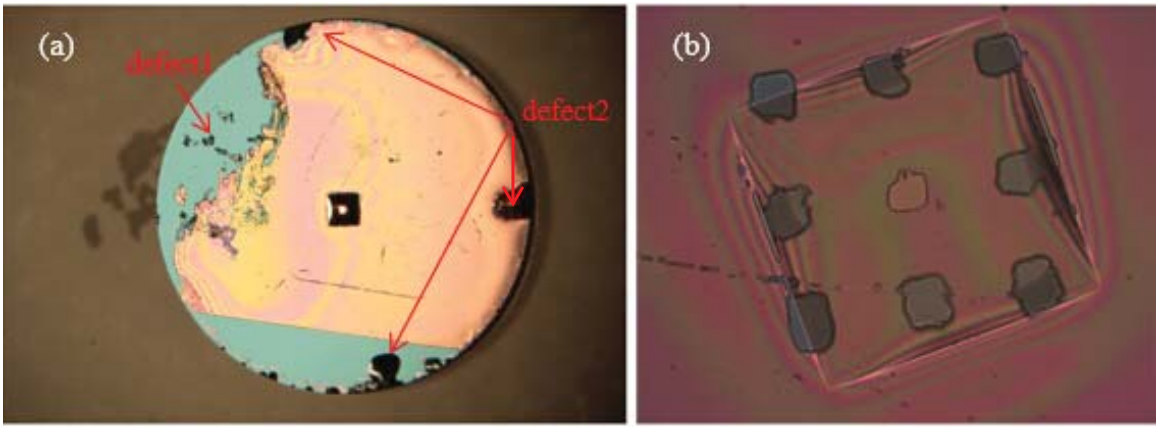

Fig.4.11 *Patterned micro-plasma electrode (a) top view of the electrode, defect1 is transferred from lithography mask, defect2 is produced by Ted Pella Inc. fabrication process (b) localized view of observation area, the misalignment of window pattern is produced because no alignment mark was prepared on the substrate and the substrate is very small.*

4.4. Electrodes without pattern

Considered the low yield and high expense of the complex electrodes pattern transfer process, four sample electrodes were reserved from copper deposition process (***Fig. 4.6***) without the electrode pattern transfer process for ex-situ plasma generation experiments.

4.5. Plasma chip fabrication result

As shown in ***Fig.4.11 (b)***, the electrode pattern was transferred on to the copper thin film layer on the top of silicon nitride TEM window. Unfortunately, the alignment between the copper pattern and the silicon opening was poor because the size of the substrate was only 3mm in diameter and there was no alignment mark prepared on it. Fortunately, the silicon nitride layer survived through the entire fabrication process.

Lithography pattern transfer process can transfer any feature on a mask to the substrate. Thus, the defects on the mask (***Fig.4.3 (b)***) were transferred onto the copper electrode (***Fig.4.11 (a)***) through lithography process, which is not desired

The electrode pattern was misaligned to the silicon opening, which could be a problem for doing in-situ TEM observation if the Cu layer blocks the TEM e-beam. A path through the plasma chip needs to be reserved for the TEM electron beam for observation purposes. The misaligned electrode can block the electron beam and cause loss of image in TEM imaging.

The misalignment problem was caused by the small substrate and no alignment mark was patterned on the substrate prior to copper electrode pattern transfer. To solve the problem, the process may need to be start over from a larger silicon substrate, such as a 4 inch silicon wafer, where alignment mark can be patterned on it.

5. Ex-situ Plasma Generation Experiment Using the Fabricated Microchip

5.1. Electrodes mounting and wiring

Both patterned and un-patterned plasma chips were mounted to the glass slide for wire bonding and ex-situ plasma experiment. Two slides was affixed with double-sided tape of 3mm width, 1.5cm length and 100um thickness were put on to the center of glass slide in parallel with a gap distance of 500μm.

A single electrode of the plasma chip was bonded onto the double-sided tape with its silicon substrate facing the glass slide and its observation area falls into the gap between the two pieces of parallel double-sided tape. The observation area with the patterned electrode was aligned in parallel to the longer edge of glass slide.

An American Wire Gauge 38 (AWG38) copper wire with insulating coating was used for electric connection for the plasma chips. The insulating layer on the tip was first striped and then bonded closely to the side of fabricated TEM plasma electrode with double-sided tape. Then a little bit of conductive glue was applied to the tip of the copper wire to improve conductivity. Then electrodes were marked as anode and cathode separately.

A PVC dielectric ring structure was used to cover the edges of the plasma chips and the connection part of the copper wire and the chip on the cathode side. The PVC ring space had a thickness of 60 μm and its dielectric strength was 544 V/mil (1mil=25.4μm). Spacer with about 660 μm thickness was bonded to the two ends of the positive glass slides. Then two glass slides were aligned and bonded together with their electrodes situated face to face by using transparent tape to form the parallel plate Ex-Situ plasma test unit (***Fig. 5.1***). The gap distance (*d*) of unit was adjusted to 60 μm.

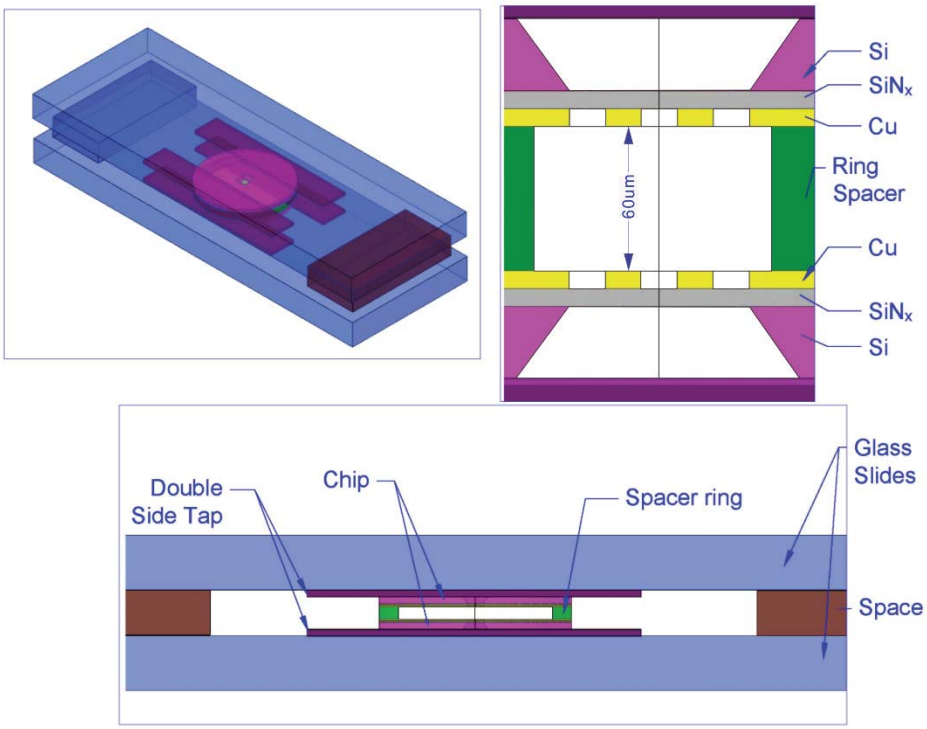

Fig.5.1 *diagram of silicon TEM plasma chip used in the ex-situ test*

5.2. Electric circuit setup

To ignite plasma in the plasma chip, an external electrical system is required to supply high voltage for the chip. To avoid interruption to the TEM electron beam, the electric field employed to ignite plasma should be in the same direction with the TEM electron beam current. The current applied to the ignited plasma must be limited to 1-2 mA in order to extend the lifetime of the plasma chip.

The electric circuit consisted with a high voltage module, a 10 kΩ potentiometer, a 1:10 voltage divider, a voltmeter, the test unit, a 5 volts DC power adaptor, and 12 volts DC power adaptor. The high voltage module is able to generate DC voltage in the range 0-2000 V and its output voltage is adjusted by the 10 kΩ potentiometer (***Fig.5.2***). The high

voltage module has a current limiting mechanic, which will limit the current to 2mA to protect the circuit.

The plasma chip was connected directly to the high voltage output and the voltmeter was connected to the high voltage output through the voltage divider. The 5 volts DC power adaptor provides power for the voltmeter and the 12 volts DC power adaptor provides power for the high voltage module. The circuit schematic is presented in Appendix 9.2.

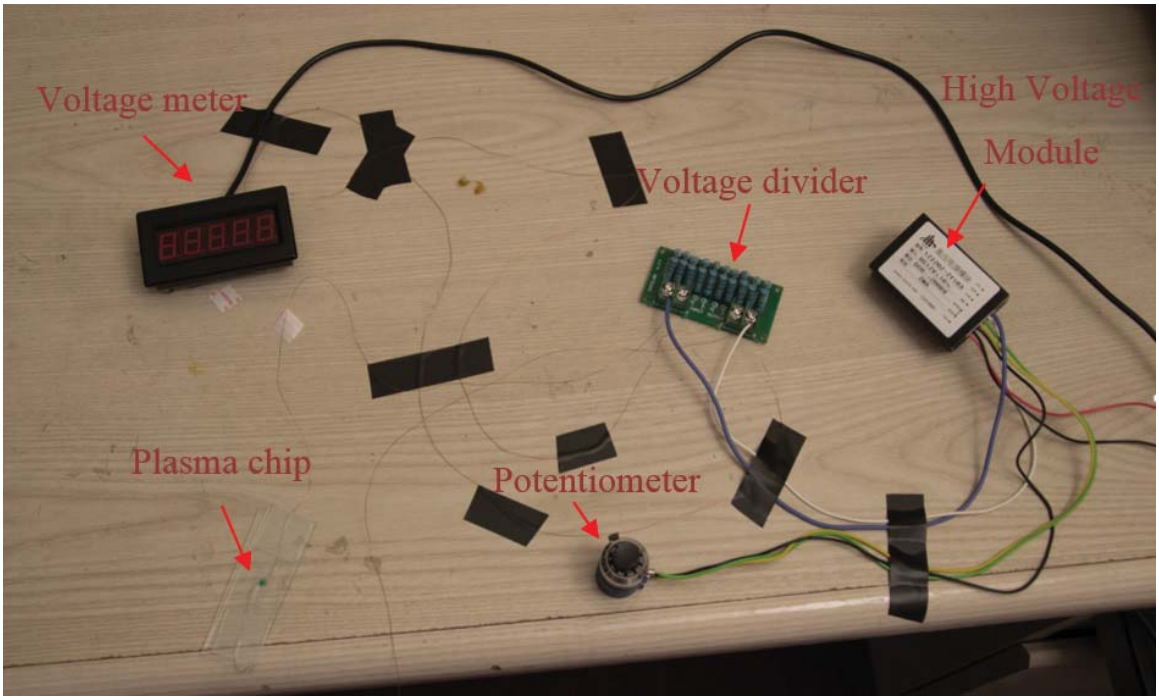

Fig.5.2 *High voltage circuit setup for ex-situ plasma test*

5.3. Ex-situ plasma generation and result

After connecting the plasma chip into the high voltage circuit, the voltage was increased gradually until the plasma was ignited. The breakdown voltage and the plasma sustain voltage was then recorded. A camera set on the side of the experiment table was used to capture the images when plasma was generated. The experiment was carried out on a well-insulated table to avoid unexpected current leaking.

The plasma was ignited successfully by an un-patterned plasma chip at 590 volts ± 10 volts, which is close to the prediction of the Paschen's Curve (570 volts at 60µm gap distance). The voltage dropped to 485 volts±10volts after the plasma was ignited due to the current protection function of the high voltage module. Bright blue-violet glow discharge was observed between the plasma chips via the naked eye and captured by a camera (***Fig. 5.3***). After 15 seconds of constant plasma generation, the circuit was cut off and the chip was disassembled for SEM characterization.

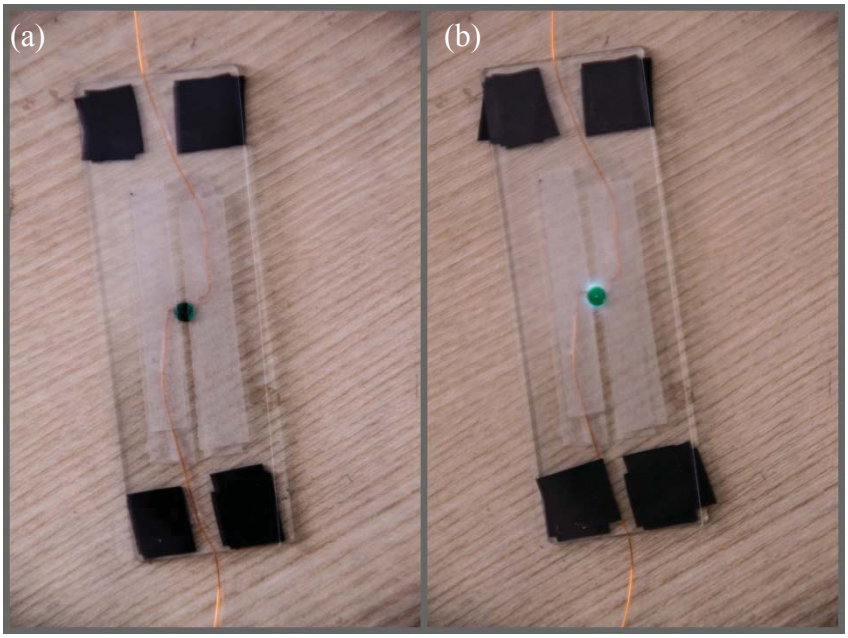

Fig.5.3 *Plasma Chip before (a) and after (b) plasma ignition*

5.4. SEM and EDS characterization for the post plasma processed plasma chip

SEM images were acquired for the surface of both positive and negative electrodes of the plasma chip at 15kv electron acceleration voltage. Etching and melting phenomenon was observed on both positive and negative electrodes. However, etching phenomenon was more obvious on the negative electrode (***Fig.5.4***), while the larger dendrites were only seen on positive electrode (***Fig.5.5***). Subsequent EDS quantitate analysis showed that about 10% of copper was oxidized during the plasma process ((***Fig.5.6***).

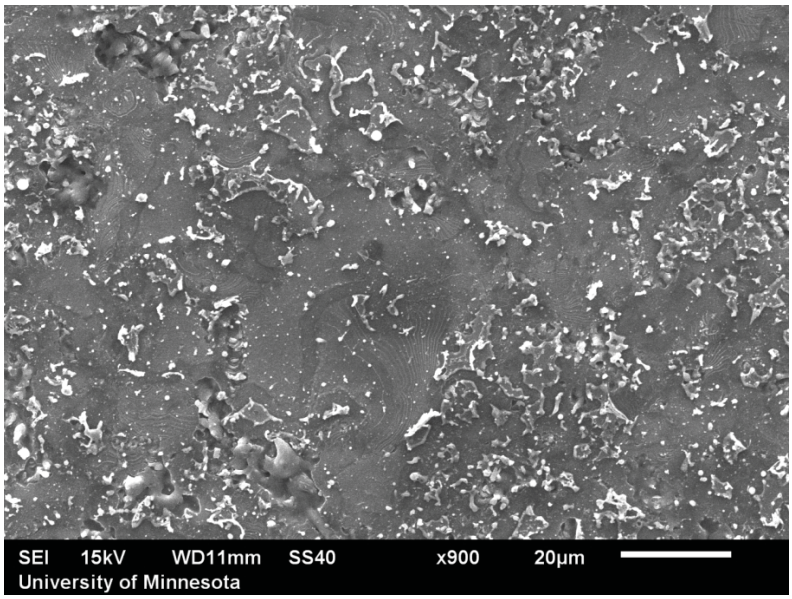

Fig.5.4 *SEM image for negative electrode of the plasma chip, both etching and deposition appears on the electrode*

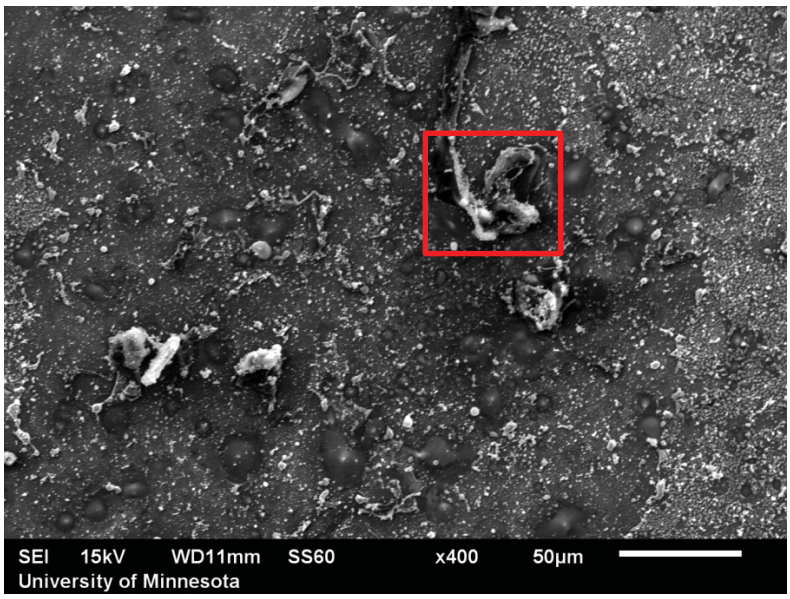

Fig.5.5 *SEM image for Positive electrode of the plasma chip, large dendrites were found formed only on positive electrode, which is an indicator of more deposition occur on positive electrode; the region marked in red was used for EDS analysis*

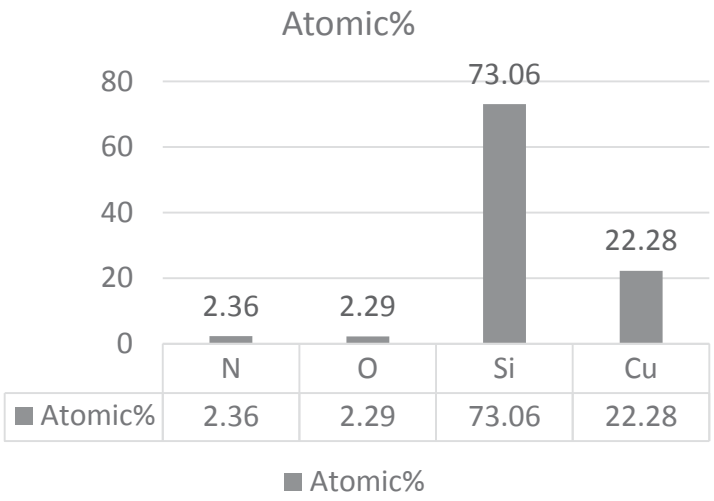

Fig.5.6 *EDS quantitative analysis for region marked in red in* ***Fig.5.5****, the result indicate a small part of Cu is oxidized during plasma process*

6. Future Work

6.1. Development of experimental setup for evaluating the performance of plasma microcell in vacuum

The plasma microcell is eventually designed for TEM observation of plasma material reactions. The plasma microcell device need to have the ability to operate in high vacuum environment. Thus a vacuum test of the plasma microcell system is required.

To move the plasma microcell to vacuum environment, a chip case (***Fig.6.1 (a)***) need to be design and prepared. The functionality of the case is to provide reliable gas sealing to the plasma microcell and to give addition protection to the sophisticated silicon based chip. The chip case should have a window on the top and bottom to allow observation. The window should have a diameter smaller than the chip (3mm) to allow mounting of the chip. Viton O-rings may be used for gas sealing between plasma chips and the chip case and the between two half chip cases (***Fig.6.1 (a)***). Polymer glue may be applied to the surface of Viton O-rings to prevent gas leaking.

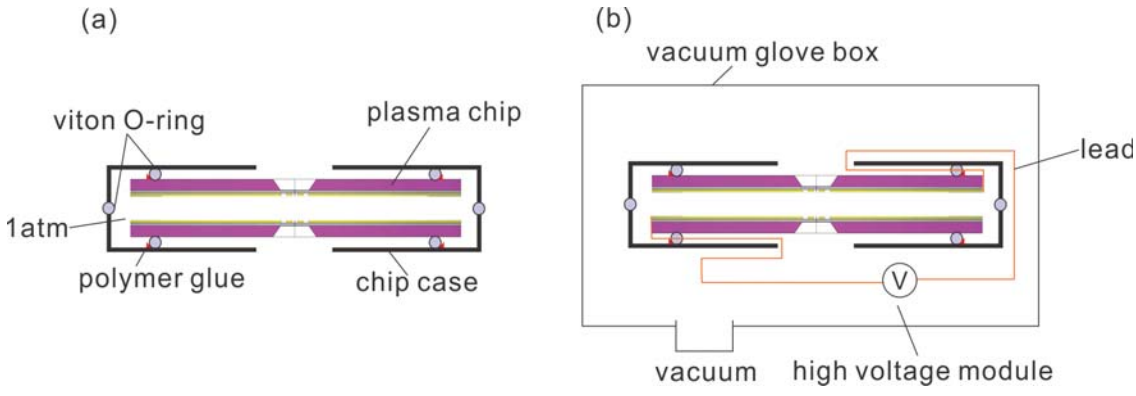

Fig.6.1 *plasma microcell design for vacuum experiment (a) plasma microcell chip case and chip mounting (b) vacuum plasma ignition experiment setup in a vacuum glove box*

After sealing the plasma microcell in air environment (for air plasma ignition), the system should be moved in a glove box to allow operation test under vacuum environment (***Fig.6.1 (b)***). Then the glove box should be pumped down and the plasma ignited by applying 590±10 V DC voltage. Because the gas environment sealed in the plasma microcell is the same with the ex-situ experiment discussed in Chapter 5, the plasma should be ignited with the same voltage (590±10 V). If the plasma is ignited, the sealing of the plasma microcell is verified. If the plasma is not ignited, one needs to check the device to locate leaking spots and to make improvement accordingly.

6.2. In-situ TEM holder development

To be implemented into TEM, a silicon-based plasma chip with batter accuracy of alignment and fewer defects need to be fabricated, because misalignment of electrodes may cause scattering of the TEM electron beam or even block the observation area. This will require preparation of a new lithographic mask and re-designed process flow starting from a 200 μm thick 4-inch wafer. The margin on the wafer edge must be reserved for any transportation operations and imperfect spin coating to protect the device being fabricated.

A structural package for holding the microchip also needs to be prepared to enable handling with TEM holders, sealing the environmental gas, and to provide reliable wire bonding support to the chip. The package needs to meet the dimension requirements of the TEM sample holder used in the high vacuum TEM chamber (***Fig. 6.2***).

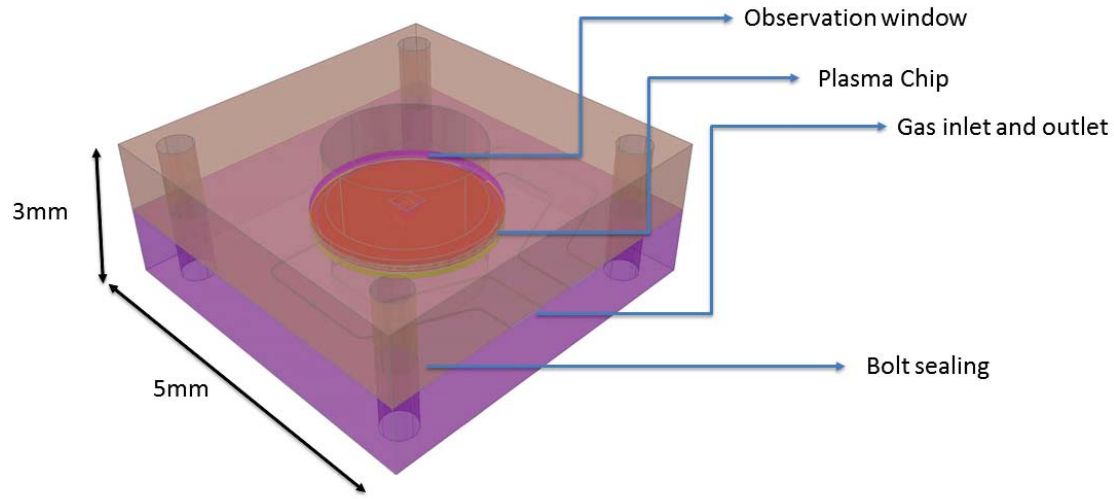

Fig.6.2 *Concept design of the plasma chip case, the case should be made in plastic and bolt bonding is used to sealing the package; Gas inlet and outlet can enable research on plasma of different gases and chemical compositions*

The structural support needs to be set up between the two copper electrodes to confine the gas used for plasma processing research. Because the sealing of the environmental cell holds a strong electric field between the electrodes while generating plasma, the dielectric property of the sealing material must be good to withstand up to 10^6 volt/meter electric field. It is also desired that the material has a high flame point to avoid any carbon contamination generated during the plasma process.

The chip may be bonded thermally to form the environmental cell. To research argon plasma, the enclosure process of environmental cell should be done in an argon glove box. The two copper electrodes need to be aligned to ensure the transparency for TEM electron beam.

After chip bonding, copper wires need to be attached to the sides of the electrodes. Because of conformal coating of DC sputtering deposition, the copper layer will also cover the side of the silicon chip and thus the connection can be made at the side of the chip. Conductive glue may be used to reduce the difficulty of doing traditional hot soldering on such a small device.

7. Conclusion

By doing Mont Carlo simulation, we find that silicon nitride thin film has very low scattering effect on 200keV TEM e-beam. Only 4.7% of electrons in the high energy e-beam was scattered during penetration process. Theoretical calculation shown high energy e-beam will benefit gas molecular dissociation and ionization. Paschen's Curve was plotted to predict the breakdown voltage and choose the minimum distance between electrodes in order to reduce electron beam scattering.

Considering the prediction of Paschen's Curve, electron scattering Mont Carlo simulation, theoretical calculations and fabrication process, we chose to use 60μm electrodes gap distance and 50nm silicon nitride thin film as observation window material. The silicon nitride thin film window structure was simulated by COMSOL Multiphysics® and the simulation result shown that the structure is capable to hold 1 atm pressure under high vacuum condition.

According to the analysis and design, plasma microchip was fabricated starting from Ted Pella® silicon nitride TEM windows by using microfabrication process. Although some defects on the copper electrodes were produced in the fabrication process because of defective lithography mask, the functionality of the plasma chip used for in-situ TEM characterization was demonstrated.

Ex-situ plasma was generated in the plasma microcell without electrodes patterning at 590±10volts, which is similar to the Paschen's curve prediction. The post plasma processed Cu electrodes were analyzed by SEM and EDS. SEM observation found dendrite formation on positive electrode. Both deposition and etching effect were found on both positive and negative electrodes. EDS analysis found CuO formation on the dendrites region.

Reference

1. Fridman A, Kennedy LA. Plasma Physics and Engineering. New York: Taylor&Francis; 2004.
2. Herink G, Solli DR, Gulde M, Ropers C. Field-driven photoemission from nanostructures quenches the quiver motion. Nature 2012;483(7388):190-193.
3. Council NR. Plasma Science: Advancing Knowledge in the National Interest. Washington, DC: The National Academies Press; 2007.
4. NASA. Spurting Plasma 2014.
5. Woo J-C, Choi C-A, Kim C-I. The Fabrication of an Applicative Device for Trench Width and Depth Using Inductively Coupled Plasma and the Bulk Silicon Etching Process. Transactions on Electrical and Electronic Materials 2014;15(1):49-54.
6. D'Emic CP, Chan KK, Blum J. Deep trench plasma etching of single crystal silicon using SF6/O2 gas mixtures. Journal of Vacuum Science & Technology B 1992;10(3):1105-1110.
7. Fedder GK, Santhanam S, Reed ML, Eagle SC, Guillou DF, Lu MSC, Carley LR. Laminated high-aspect-ratio microstructures in a conventional CMOS process. 1996 11-15 Feb 1996. p 13-18.
8. Gomez S, Jun Belen R, Kiehlbauch M, Aydil ES. Etching of high aspect ratio structures in Si using SF6/O2 plasma. Journal of Vacuum Science & Technology A 2004;22(3):606-615.
9. Westerheim AC, Labun AH, Dubash JH, Arnold JC, Sawin HH, Yu-Wang V. Substrate bias effects in high-aspect-ratio SiO2 contact etching using an inductively coupled plasma reactor. Journal of Vacuum Science & Technology A: Vacuum, Surfaces, and Films 1995;13(3):853-858.
10. Schutze A, Jeong JY, Babayan SE, Park J, Selwyn GS, Hicks RF. The atmospheric-pressure plasma jet: a review and comparison to other plasma sources. Plasma Science, IEEE Transactions on 1998;26(6):1685-1694.
11. Tricot S, Boulmer-Leborgne C, Nistor M, Millon E, Perrière J. Dynamics of a pulsed-electron beam induced plasma: application to the growth of zinc oxide thin films. Journal of Physics D: Applied Physics 2008;41(17):175205.
12. Shah A, Torres P, Tscharner R, Wyrsch N, Keppner H. Photovoltaic Technology: The Case for Thin-Film Solar Cells. Science 1999;285(5428):692-698.
13. Tong M, Dai G, Wu Y, He X, Gao D. WO3 thin film prepared by PECVD technique and its gas sensing properties to NO2. Journal of Materials Science 2001;36(10):2535-2538.
14. Sunkara MK, Sharma S, Miranda R, Lian G, Dickey EC. Bulk synthesis of silicon nanowires using a low-temperature vapor–liquid–solid method. Applied Physics Letters 2001;79(10):1546-1548.
15. Cantalini C, Valentini L, Armentano I, Lozzi L, Kenny JM, Santucci S. Sensitivity to NO2 and cross-sensitivity analysis to NH3, ethanol and humidity of

carbon nanotubes thin film prepared by PECVD. Sensors and Actuators B: Chemical 2003;95(1–3):195-202.
16. Meyyappan M, Lance D, Alan C, David H. Carbon nanotube growth by PECVD: a review. Plasma Sources Science and Technology 2003;12(2):205.
17. Kim H-H. Nonthermal Plasma Processing for Air-Pollution Control: A Historical Review, Current Issues, and Future Prospects. Plasma Processes and Polymers 2004;1(2):91-110.
18. Mizuno A, Ito H. Basic performance of an electrostatically augmented filter consisting of a packed ferroelectric pellet layer. Journal of Electrostatics 1990;25(1):97-107.
19. Rovagnati B, Mashayek F. A kinetic model to study film deposition during dusty plasma chemical vapor deposition process. Journal of Applied Physics 2009;105(6):063303.
20. Ghassemi H, Au M, Chen N, Heiden PA, Yassar RS. Real-time observation of lithium fibers growth inside a nanoscale lithium-ion battery. Applied Physics Letters 2011;99(12):123113.
21. Bar-Sadan M, Barthel J, Shtrikman H, Houben L. Direct Imaging of Single Au Atoms Within GaAs Nanowires. Nano Letters 2012;12(5):2352-2356.
22. Hirata A, Guan P, Fujita T, Hirotsu Y, Inoue A, Yavari AR, Sakurai T, Chen M. Direct observation of local atomic order in a metallic glass. Nat Mater 2011;10(1):28-33.
23. Wilson CG, Gianchandani YB. Silicon micromachining using in situ DC microplasmas. Journal of Microelectromechanical Systems 2001;10(1):50-54.
24. Miyazoe H, Utke I, Kikuchi H, Kiriu S, Friedli V, Michler J, Terashima K. Improving the metallic content of focused electron beam-induced deposits by a scanning electron microscope integrated hydrogen-argon microplasma generator. Journal of Vacuum Science & Technology B: Microelectronics and Nanometer Structures 2010;28(4):744.
25. Sun L, Noh KW, Wen J-G, Dillon SJ. In Situ Transmission Electron Microscopy Observation of Silver Oxidation in Ionized/Atomic Gas. Langmuir 2011;27(23):14201-14206.
26. Tai K, Houlahan TJ, Jr., Eden JG, Dillon SJ. Integration of microplasma with transmission electron microscopy: Real-time observation of gold sputtering and island formation. Scientific Reports 2013;3:1325.
27. Stutzin GC, Rózsa K, Gallagher A. Deposition rates in direct current diode sputtering. Journal of Vacuum Science & Technology A 1993;11(3):647-656.
28. Chen FF. Introduction to Plasma Physics and Controlled Fusion. Springer US; 1984.
29. Lieberman MA, Lichtenberg AJ. Principles of Plasma Discharges and Materials Processing. Hoboken, New Jersey: John Wiley&Sons, Inc.; 2005.
30. Braithwaite NSJ. Introduction to gas discharges. Plasma Sources Sci. Technol 2000;9:11.

31. Paschen F. Ueber die zum Funkenübergang in Luft, Wasserstoff und Kohlensäure bei verschiedenen Drucken erforderliche Potentialdifferenz. Annalen der Physik 1889;273(5):69-96.
32. Cobine JD. Gaseous Conductors: Theory and Engineering Application. New York: Dover Publications, Inc.; 1958.
33. Young HD, Freedman RA. Sears & Zemansky's University Physics. Addison-Wesley; 2011.
34. Velchev I, Hogervorst W, Ubachs W. Precision VUV spectroscopy of Ar I at 105 nm. Journal of Physics B: Atomic, Molecular and Optical Physics 1999;32(17):L511.
35. Vasenkov AV. Nonequilibrium argon plasma generated by an electron beam. Physical Review E 1998;57(2):2212-2221.
36. Kadoun A, Belkorissat R, Khelifa B, Mathieu C. Comparative study of electron beam–gas interaction in an SEM operating at pressures up to 300Pa. Vacuum 2003;69(4):537-543.
37. Mansour O, Aidaoui K, Kadoun A-E-D, Khouchaf L, Mathieu C. Monte Carlo simulation of the electron beam scattering under gas mixtures environment in an HPSEM at low energy. Vacuum 2010;84(4):458-463.
38. Mansour O, Kadoun A, Khouchaf L, Mathieu C. Monte Carlo simulation of the electron beam scattering under water vapor environment at low energy. Vacuum 2013;87(0):11-15.
39. Mathieu C. The beam-gas and signal-gas interactions in the variable pressure scanning electron microscope. Scanning Microscopy 1999;13(1).
40. Danilatos GD. Electron scattering cross-section measurements in ESEM. Micron 2013;45(0):1-16.
41. Lenz FL. Zur Streuung mittelschneller Elektronen in kleinste Winkel. Zeitschrift für Naturforschung A 1954;9.
42. Danilatos GD. Advances in Electronics and Electron Physics. San Diego: Academic Press, Inc; 1990.
43. Wight SA, Konicek AR. Electron scattering cross section measurements in a variable pressure scanning electron microscope. Micron 2012;43(9):985-991.
44. Drouin D, Couture AR, Gauvin R, Hovington P, Homy P, Demers H. Casino. 3.22011.
45. Demers H, Horny P, Gauvin R, Lifshin E. Win X-Ray
46. Shackelford JF, Alexander W. CRC Materials Science and Engineering Handbook. CRC press; 2000.
47. Ali MA, Kim Y-K, Hwang W, Weinberger NM, Rudd ME. Electron-impact total ionization cross sections of silicon and germanium hydrides. The Journal of Chemical Physics 1997;106(23):9602-9608.
48. Simões S, Calinas R, Vieira MT, Vieira MF, Ferreira PJ. In situ TEM study of grain growth in nanocrystalline copper thin films. Nanotechnology 2010;21(14):145701.
49. Kaushik A, Kahn H, Heuer AH. Wafer-level mechanical characterization of silicon nitride MEMS. Journal of Microelectromechanical Systems 2005;14(2):359-367.

50. Chen S-J, Choe Y, Baumgartel L, Lin A, Kim ES. Edge-released, piezoelectric MEMS acoustic transducers in array configuration. Journal of Micromechanics and Microengineering 2012;22.
51. Ganji BA. Design and Fabrication of a Novel MEMS Silicon Microphone. In: Basu S, editor. Crystalline Silicon – Properties and Uses: InTech; 2011.

8. Appendices

8.1. Matlab® Code for Paschen's Curve

```
%*******************************
%"PaschenCurve_Argon_Copper.m":
%By Xuebo Cui for Master Thesis in Michigan Tech April4th, 2014
%*******************************

%parameter define:
%A,B for Air and Gamma is the second ionization coefficient for Copper
%electrode;

gamma=0.025;
A=14.6;
B=365;

%set evalution range and sample density
%lower pd range has higher sample density and higher pd range has lower
%sample density
%pd= presure* gap distance

pd_lower=0.01:0.001:1;
pd_higher=2:1:1000;
pd=[pd_lower pd_higher];

%apply paschen's law: write equation
t1=B.*pd;
t2=log(pd.*A);
t3=log(log(1+gamma^(-1)));
bdvolt=t1./(t2-t3);

%covert Torr*cm to Torr*mm
%plot breakdown voltage(bdvolt) vs. pressure*gap distance(pd) in log %scale:

loglog(pd.*10,bdvolt,'*k');
axis([1 1e4 100 1e5]);
```

```
%annote the graph
title('Paschens Curve for Air and Copper');
xlabel('pd (Torr*mm)');
ylabel('V_b, Breakdown Voltage (volts)');

text(9,8e3,['A=14.6(Torr*cm)^(-1)']);
text(9,5e3,['B=365 V/(Torr*cm)']);
text(9,3e3,['gamma=0.025']);

colordef white;

%Citation:
%Parameters A, B and gamma cite from: Jame Dillon Cobine,Gaseous Conductor: Theary
and Engineering
%Application 1958 Dover Publication,Inc,

%****************Code End Here****************
```

8.2. High Voltage Circuit Schematic

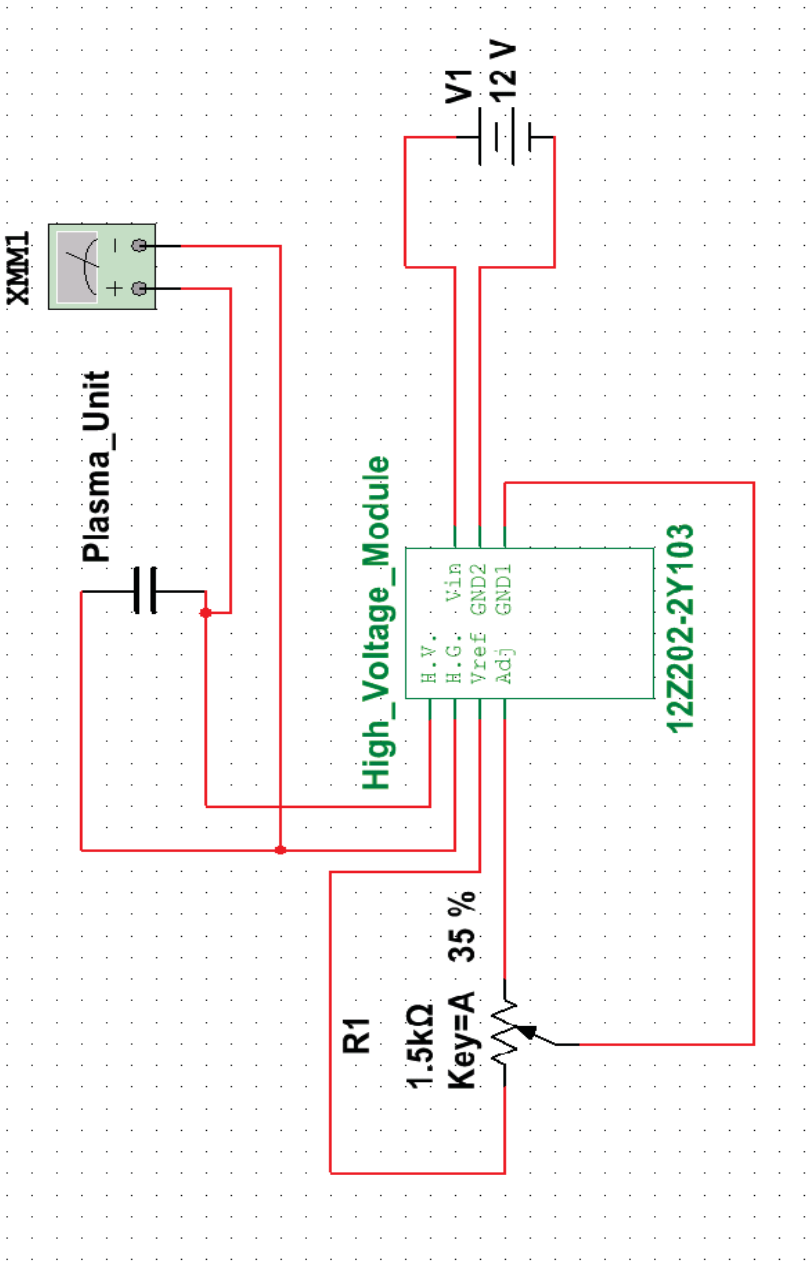

Fig.8.1 *High voltage circuit configuration*

8.3. COMSOL Simulation for Silicon Substrate Deformation

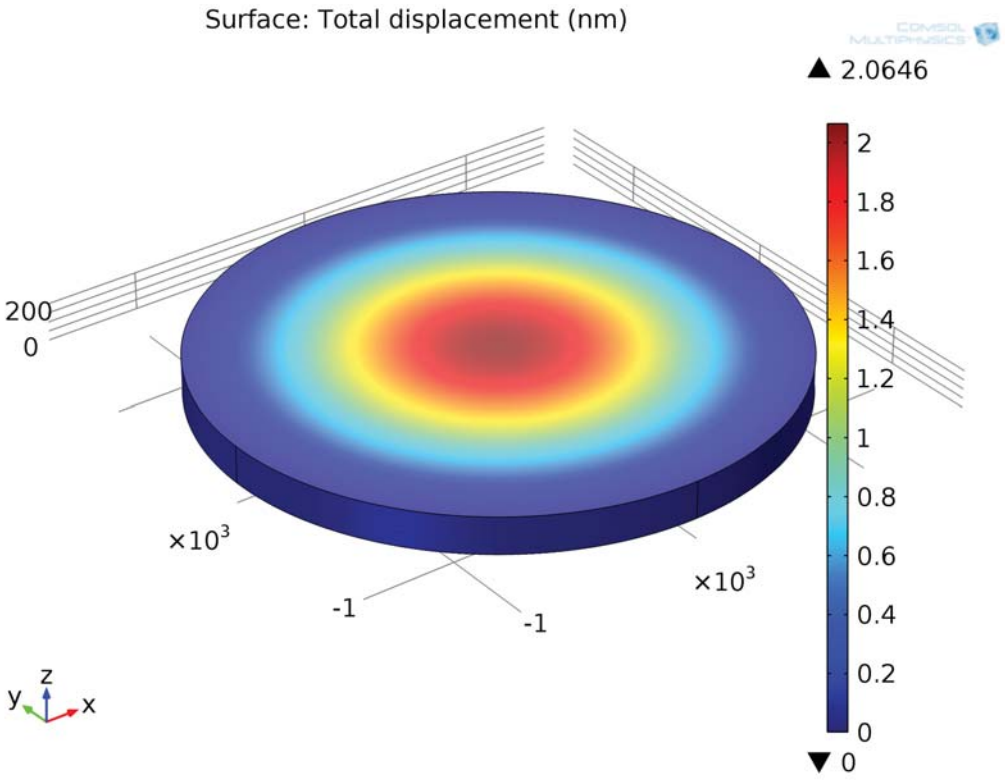

Fig.8.2 *3D total displacement of silicon substrate under 1atm pressure*